THE UNIVERSITY OF CHICAGO

METASTABLE TRIPLET STATES AS SPIN SENSORS

A DISSERTATION SUBMITTED TO
THE FACULTY OF THE PRITZKER SCHOOL OF MOLECULAR ENGINEERING
IN CANDIDACY FOR THE DEGREE OF
DOCTOR OF PHILOSOPHY

BY
JACOB SAMUEL FEDER

CHICAGO, ILLINOIS
JUNE 2025

Copyright 2025 Jacob Samuel Feder

All Rights Reserved

For my family and friends.

If you want to go far, don't go alone.

ABSTRACT

Here, we demonstrate the use of the enhanced yellow fluorescent protein (EYFP) as an optically-addressable spin sensor. This thesis details the background, experimental techniques, and measurements used to characterize the properties of this novel sensor. I hope it may be of use to future experimentalists in their study of metastable triplet systems.

TABLE OF CONTENTS

ABSTRACT v

LIST OF FIGURES ix

1 SPECTROSCOPY 1
1.1 Molecular states 2
1.1.1 Thermal state population 2
1.1.2 Orbital states 3
1.1.3 Vibrational states 4
1.1.4 Spin states 4
1.2 Photoexcitation 4
1.3 Relaxation 5
1.4 Photoluminescence 5
1.4.1 Fluorescence 6
1.4.2 Phosphorescence 6
1.5 Linewidth broadening 6
1.5.1 Homogeneous broadening 7
1.5.2 Inhomogeneous broadening 7

2 SPECTROSCOPY TECHNIQUES 8
2.1 Absorption 8
2.2 Emission 9
2.3 Transient absorption 10
2.4 Electron paramagnetic resonance 11
2.5 Optically-detected magnetic resonance 12

3 FLUORESCENT PROTEINS 13
3.1 Photophysics 13
3.2 Directed evolution 14
3.3 Metastable triplet state 15
3.4 Optically-activated delayed fluorescence 15

4 OPTICS 17
4.1 Polarization 18
4.2 Reflection & refraction 18
4.3 Ray optics 20
4.3.1 Paraxial approximation 20
4.4 Ray-transfer matrices 21
4.5 Basic optical components 22
4.5.1 Lenses 22
4.5.2 Mirrors 23
4.5.3 Dichroic mirrors & filters 24

4.6 Beam expander . . . 24
4.7 Microscope . . . 25
4.8 Aberrations . . . 25
4.8.1 Spherical . . . 26
4.8.2 Chromatic . . . 26

5 EXPERIMENTAL HARDWARE . . . 27
5.1 Mechanics . . . 27
5.1.1 Cryogenics . . . 27
5.1.2 Sample mount . . . 29
5.1.3 Sample coverslip . . . 29
5.2 Optics . . . 30
5.2.1 Lasers . . . 30
5.2.2 Acousto-optic modulators . . . 30
5.2.3 Detectors . . . 31
5.3 Electronics . . . 31
5.3.1 Power distribution . . . 32
5.3.2 AOM driver PCB . . . 33
5.3.3 Microwave electronics . . . 36

6 PULSE GENERATION . . . 37
6.1 RFSoC . . . 37
6.1.1 RF outputs . . . 38
6.1.2 RF inputs . . . 38
6.1.3 Digital outputs . . . 38
6.2 Quantum instrumentation control kit (QICK) . . . 38
6.2.1 QICK-SPIN . . . 40
6.2.2 Time tagger . . . 40
6.2.3 RF input buffer PCB . . . 41
6.2.4 Digital output buffer PCB . . . 43
6.2.5 QICK pulse compiler . . . 44

7 CONTROL SOFTWARE (NSPYRE) . . . 46
7.1 Instrument control . . . 46
7.1.1 InstrumentServer . . . 47
7.1.2 InstrumentManager . . . 47
7.2 Data processing . . . 48
7.2.1 DataSource . . . 48
7.2.2 DataSink . . . 49
7.2.3 StreamingList . . . 49
7.3 Graphical user interface . . . 50

8 FLUORESCENT-PROTEIN SPIN QUBITS 52
8.1 Protein qubit and spin readout 54
8.2 Optically-detected magnetic resonance 57
8.3 Qubit coherence 59
8.4 Operation at room temperature 63
8.5 Qubit sensor expressed in mammalian cells 64
8.6 Discussion and outlook 65
8.7 Protein expression and purification 68
8.8 EYFP expression in mammalian cells 69
8.9 Experimental methods 70
8.10 Data analysis 70
8.11 Sample degradation 71
8.12 Computational methods 71
8.13 TDDFT and ZFS calculations 72
8.14 Simulation magnetic resonance spectrum 72
8.15 Rabi simulation 73
8.16 Estimation of number of measured molecules 74
8.17 Sensitivity estimation 75
8.17.1 DC sensitivity (293 K) 76
8.17.2 AC sensitivity (80 K) 77
8.18 Limit of detection: NMR sensing 78

9 METASTABLE TRIPLET DYNAMICS 79
9.1 Initialization 79
9.1.1 3-level model 79
9.1.2 4-level model 81

REFERENCES 84

LIST OF FIGURES

1.1 Jablonski diagram 3

1.2 Linewidth broadening 7

2.1 EYFP spectra 9

3.1 EYFP structure 14

3.2 EYFP chromophore structure 14

5.1 Cryogenic sample mount CAD side 28

5.2 Cryogenic sample mount CAD top 28

5.3 Cryogenic sample mount 29

5.4 Coplanar waveguide coverslip 30

5.5 Server rack (front) 31

5.6 Server rack (back) 31

5.7 2-tone AOM driver schematic 33

5.8 2-tone AOM driver 34

6.1 RFSoC buffer PCBs 39

6.2 RFSoC ADC buffer PCB schematic 41

6.3 RFSoC ADC buffer PCB 42

6.4 RFSoC ADC balun mod 42

6.5 RFSoC ADC balun mod 42

6.6 RFSoC ADC balun mod 42

6.7 RFSoC digital output buffer PCB schematic 43

6.8 RFSoC digital output buffer PCB 44

6.9 QICK pulse compiler python code 45

6.10 QICK assembly code 45

7.1 nspyre experiment GUI 50
7.2 nspyre experiment plotting 51

8.1 Photophysics of EYFP proteins and OADF readout scheme 55
8.2 Experimental optical setup 56
8.3 Sample integrity 57
8.4 Triplet state readout 58
8.5 ODMR spectroscopy of EYFP 59
8.6 Resonance frequencies vs. magnetic field 60
8.7 Coherent control of EYFP qubits 61
8.8 Rabi oscillation simulations 62
8.9 Room temperature quantum sensing 63
8.10 Coherent control in cells 64
8.11 Cell measurements 66
8.12 Calculated D and E parameters 73
8.13 Knife-edge measurements 74
8.14 YZ transition at room temperature 75
8.15 Sensitivity estimation 76

9.1 Initialization 3-level rate equation 80
9.2 Initialization 4-level rate equation 81

CHAPTER 1

SPECTROSCOPY

The thickness of a human hair is on the order of 0.1 mm, or 100 µm. A typical molecule is about 1 nm — 100,000× smaller. An atom is around 10× smaller still. These length scales are so far beyond those that we experience in our daily lives that they can be hard to comprehend. Yet the behavior of macroscopic objects are dictated by the nanoscale interactions between these minute atoms and molecules. Chemical reactions, material properties, and living things are all subject to the laws that govern these tiny objects. How can we hope to understand these nanoscale objects and their interactions? Many approaches have been developed, but, perhaps one of the most successful, is spectroscopy.

Visible light that allows humans to see, radio- and microwave-frequency signals that wirelessly transmit data to cell phones and computers, and low-frequency fields generated by electrical relays to open and close automatic doors are all examples of electromagnetic fields. While they may seem quite disparate, these electromagnetic fields are all subject to the same physical laws. Electrical relays that hold open doors turn on and off on the order of seconds, corresponding to oscillations on the scale of Hz. The electric and magnetic fields that carry radio- and microwave-frequency signals oscillate in the MHz to GHz range, and visible light in the 100's of THz.

Spectroscopy is a tool that examines the interaction between electromagnetic fields and matter. As there is a broad range of oscillation frequencies of electromagnetic fields, as well as a broad range of ways in which these fields can interact with atoms and molecules, there are many different types of spectroscopy. Here, we will primarily concern ourselves with two pieces of the electromagnetic spectrum: one that comprises optical light, whose energy corresponds with the energy difference between orbital levels in many atoms and molecules; and one that comprises microwave signals, whose energy often corresponds with the energy difference between spin levels.

1.1 Molecular states

Atoms and molecules possess discrete, or quantized, energy levels associated with their current state. These energy levels are conveniently described by a Jablonski diagram, such as that given in figure 1.1. The states of the molecule are represented by horizontal lines. Their placement along the x-axis is arbitrary. The height above the y-axis is proportional to the energy of the state. Potential transitions between the states are indicated with arrows. The lowest-energy state in the system is termed the "ground" state.

In general, the energies of the states can be computed using the Schrödinger equation

$$\hat{H}\,|\psi\rangle = E\,|\psi\rangle \tag{1.1}$$

(provided $\hat{H}$ does not vary with time). The matrix $\hat{H}$ is called a Hamiltonian, and captures the different physical effects that contribute to the final state energies, E. The vector $|\psi\rangle$ represents the state of the system. A reader with experience with linear algebra may notice that solving this equation is an exercise in matrix diagonalization. Coming up with a Hamiltonian that accurately describes a system under study and diagonalizing that Hamiltonian is the principle tool with which we can describe the behavior of atoms and molecules.

1.1.1 Thermal state population

In a thermodynamically closed system, thermal energy creates an equilibrium between its states according to Maxwell-Boltzmann statistics. The population in each level is given by

$$\frac{N_i}{\sum_j N_j} = \frac{\exp -\frac{E_i}{k_B T}}{\sum_j \exp -\frac{E_j}{k_B T}} \tag{1.2}$$

where N_i is the population in state i, E_i is the energy of state i, k_B is the Boltzmann constant, and T is the temperature. Due to the exponential dependence on $-\frac{E_i}{k_B T}$, states

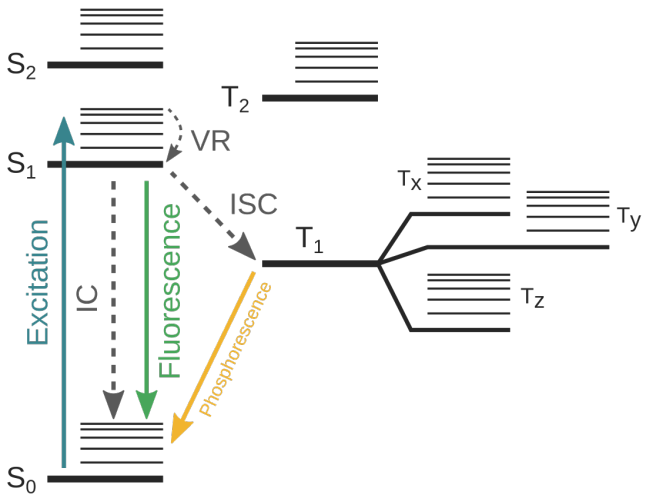


Figure 1.1: Jablonski diagram showing a molecule undergoing photoexcitation with off-resonant light. S_0 is the singlet ground state. S_1 and S_2 are singlet excited electronic states. T_1 and T_2 are triplet excited electronic states. Sublevels above each electronic state represent the manifold of vibrational levels associated with it. T_x, T_y, and T_z are spin sublevels of the T_1 state. VR indicates vibrational relaxation after undergoing photoexcitation to a vibrational sublevel of S_1. IC indicates internal conversion from the S_1 to S_0 state. ISC indicates intersystem crossing, involving a change in spin multiplicity.

whose energy above the ground state is much larger than $k_B T$ are negligibly populated.

1.1.2 Orbital states

The electrons bound to an atomic nucleus or group of nuclei in a molecule can only exist in a set of discrete states termed orbitals. Each orbital is a probability distribution of spatial positions of the electron with respect to the nuclei. Different orbitals possess different energies (as computed from the Hamiltonion). The energy difference between an orbital and that of the next highest energy is often in the $\sim$ eV range, which corresponds to photons at optical wavelengths.

1.1.3 Vibrational states

Molecules are composed of multiple atoms, whose chemical bonds determine their relative positions. However, they can be perturbed by kinetic energy, which causes the atoms to oscillate with respect to each other. In turn, these oscillations perturb the electron orbitals. A molecule with many atoms has many different vibrational modes, each with its own associated energy. In figure 1.1, each orbital level possess a vibronic sideband of energy levels that correspond to the orbital state combined with all of the associated vibrational modes of the molecule. The energy of these vibrations span a large range of oscillation frequencies from $\sim$ GHz to 100 THz.

1.1.4 Spin states

Spin is a fundamental property of particles like electrons, protons, and neutrons, which all possess a spin of 1/2. Larger collections of these particles in an atom or molecule can possess higher spin numbers. Spins interact with magnetic fields, and are one of the primary sources of magnetic effects in molecules and materials. Because spin is quantized, a spin 1/2 can either be a spin up, or spin down. In general, the energy difference between the different spin states can have intrinsic contributions such as dipole-dipole interactions and spin-orbit coupling, as well as extrinsic contributions such as an external magnetic field. For the systems considered here, the energy-level splittings of the spin sublevels lie in the range of $0 - 10$ GHz, which are easily accessed with RF and microwave electronics.

1.2 Photoexcitation

When an electromagnetic field impinges on a molecule and its energy corresponds with the energy difference between two states of the molecule, there is a chance that molecule will absorb the photon associated with the field, and undergo a transition from the lower to

higher energy state. This process is termed photoexcitation. Given a continuous stream of monochromatic photons, the rate at which photoexcitation occurs is given by

$$k = \frac{\sigma I}{hf}, \tag{1.3}$$

where k is the rate in Hz, I the light intensity, f the light frequency, h Planck's constant, and σ the absorption cross section, which depends strongly on the physics of the molecular system and the interaction mechanism.

1.3 Relaxation

Molecules can spontaneously transition from a higher-energy state to a lower-energy state, termed relaxation. Given a rate of relaxation, k, $1/k = \tau$ is the lifetime of the higher-energy state. The population in this state, P, as a function of time, t, is given by a simple exponential decay

$$P = e^{-t/\tau}. \tag{1.4}$$

Relaxation can be radiative, which emits a photon, or non-radiative, which does not. Radiative relaxation is most commonly seen for transitions from excited to ground orbital states, and usually have $\sim$ ns-scale lifetimes. These transitions can also be non-radiative, in which case they are called internal conversion and have ps-ns scale lifetimes. Relaxation from higher- to lower-energy vibrational states are non-radiative, and typically have lifetimes of $\sim$ ps. Finally, intersystem crossing is a transition that involves a change in spin multiplicity.

1.4 Photoluminescence

Photoluminescence (PL) is the light emitted due to radiative relaxation from a molecule after undergoing photoexcitation. Depending on the time scale of the PL, it has different

names.

1.4.1 Fluorescence

Fluorescence refers to fast time-scale radiative relaxation. Typically, it involves a transition that is "allowed" (has a non-zero rate) by the selection rules of the system Hamiltonian. In figure 1.1, the transition from S_1 to S_0 emits fluorescence.

1.4.2 Phosphorescence

Phosphorescence refers to slow time-scale radiative relaxation. Typically, it involves a transition that is "forbidden" (has an approximately zero rate) by the selection rules of the system Hamiltonian. For example, in figure 1.1 the T_1 to S_0 transition emits phosphorescence. It is forbidden because it involves a change in spin multiplicity.

1.5 Linewidth broadening

Depending on the state of matter that a molecule is in, many different mechanisms can perturb its energy levels. These perturbations lead to a broadening of the absorption or emission transitions. For example, fluctuating electric or magnetic fields may affect the energy levels by the Stark and Zeeman effects, respectively. The stochastic nature of radiative relaxation leads to a fundamental limit on the linewidth of a transition, given by the lifetime of the higher-energy state. This "lifetime-limited" (or "Fourier-limited") linewidth has a Lorentzian profile, since it is a frequency-domain representation of the relaxation exponential decay mentioned above.

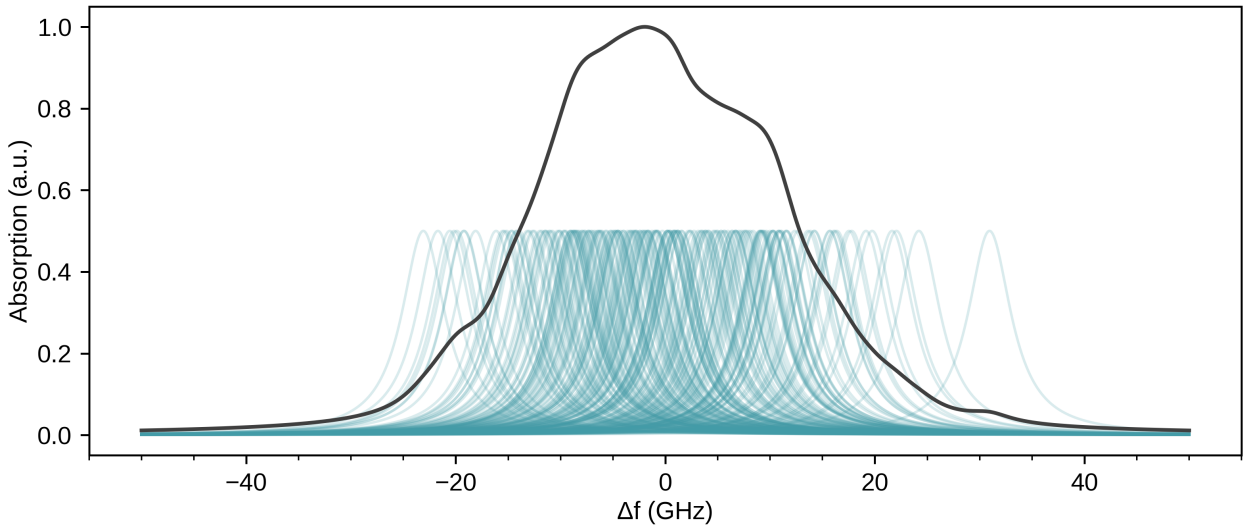


Figure 1.2: Simulation demonstrating inhomogeneous broadening. Each individual blue peak represents the absorption spectra of a single molecule, which has a linewidth given by the homogeneous linewidth. Each molecule experiences a different local environment, and thus there is a distribution of center positions of the peaks. The black peak is the sum of all individual blue peaks, whose linewidth is the inhomogeneous linewidth.

1.5.1 Homogeneous broadening

A mechanism that equally affects all molecules in an ensemble contributes to homogeneous broadening. For example, the stochastic nature of radiative relaxation is an example of homogeneous broadening, since it affects all molecules in an ensemble identically. When measuring a single molecule, its linewidth is the homogeneous linewidth.

1.5.2 Inhomogeneous broadening

A mechanism that has a different affect on the molecules across an ensemble contributes to inhomogeneous broadening. For example, in a crystalline sample, defects in the lattice create local strain in the crystal, leading to a broad range of strains throughout the sample. If a molecule were embedded in this crystal and its transitions are sensitive to strain, the strain created by the crystal defects would result in inhomogeneous broadening. Figure 1.2 demonstrates the origin of inhomogeneous broadening.

CHAPTER 2

SPECTROSCOPY TECHNIQUES

In section 1.1 we discussed the various physical effects that govern an atom's or molecule's states. The differences in energy between these levels span a huge range. For nearly any section of this range, there is a spectroscopic technique that uses electromagnetic waves to probe and extract information about the energy level structure of the molecule. Determining the energy levels can in turn provide extremely detailed information about the physical structure of the molecule, as well as its environment.

2.1 Absorption

The simplest way of probing the energy levels of a molecule is absorption spectroscopy. In a typical measurement, the energy difference between orbitals is high compared to $k_B T$, and the excitation intensity of the light source is small, so the molecules can be presumed to be primarily populating the electronic ground state. By observing the amount of light absorbed by a molecule as a function of the light's wavelength, the energy difference between the excited states and ground state can be deduced.

Figure 2.1 shows the absorption (and emission) spectra of the enhanced yellow fluorescent protein (EYFP), a fluorophore popular in bioimaging. Note that the x-axis of the absorption spectra, and many other optical spectroscopy techniques, is in units of wavelength rather than energy. EYFP has an energy-level diagram like that shown in figure 1.1. The broad absorption feature from $\sim$ 450 nm to 540 nm is a consequence of the absorption of the transition from the ground (S_0) state to the excited (S_1) state. Its large linewidth is due to two effects. First, the molecule may be excited from its ground state to a myriad of levels in the vibrational manifold of the S_1 state. Second, inhomogeneous broadening affects each of these individual vibrational states, causing them to overlap and combine into a smeared-out

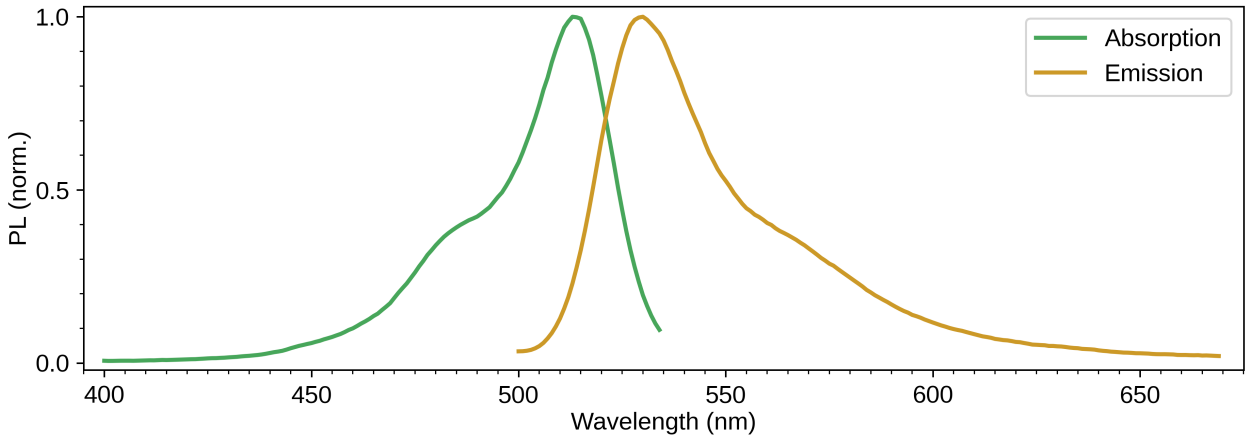


Figure 2.1: Absorption and emission spectra of EYFP [1]

feature.

A typical system for acquiring the absorption spectrum consists of a white light source, dispersive optic, and detector. The white light source emits a range of wavelengths from the ultra-violet (UV) to visible (VIS) portion of the optical spectrum, illuminating the sample. For this reason, the instrument is often called a "UV-VIS" spectrometer. The light transmitted through the sample is dispersed onto the detector, which translates the signal into a transmission spectrum.

2.2 Emission

A molecule may emit photoluminescence in the form of fluorescence (or phosphorescence). This PL can give further information about the molecule. Under off-resonant excitation, a molecule will undergo photoexcitation to a higher-energy vibrational state in an orbital excited state, then relax to the lowest-energy state within the vibrational manifold of the photoexcited state before emitting a fluorescence photon via radiative relaxation. It may populate a vibrational level within the ground state, and again relax to the ground state, dissipating thermal energy. The loss of energy in this process results in the emitted fluorescence having a lower energy (and longer wavelength) than the excitation light. The change

in wavelength between the peak of the absorption and emission spectra is called the Stokes shift. The emission spectrum of EYFP is shown in figure 2.1. It consists of a broad, smeared out feature for the same reasons as given for the absorption spectra, and a stokes shift of about 15 nm.

Collecting emission spectra is more complicated than absorption spectra. The molecule may be excited with a white light or monochromatic source like a laser. However, the excitation source is much higher power than the fluorescence, which is the main technical challenge that is addressed by a combination of techniques. Collecting light scattered back towards the source (rather than transmitted through the sample) significantly reduces the amount of laser light that reaches the detector. In order to separate the excitation and emission beams, the excitation is reflected off a dichroic mirror, and the emission is transmitted through it. Reflecting the excitation and transmitting the emission (rather than vice versa) can be important in order to avoid impurities in the dichroic mirror substrate being photoexcited and contributing to the signal. Typically, an optical filter is placed in the transmitted path after the dichroic mirror in order to further reduce the leakage of excitation light into the detector. If the excitation source is a white light, or a laser with out-of-band emission, it may be necessary to use an optical filter before reflecting off the dichroic mirror, in order to reduce any leakage of light that may interfere with the PL signal.

2.3 Transient absorption

While UV-VIS absorption spectroscopy is useful for determining the energy of excited states, it does not provide any temporal resolution. Transient absorption is a form of "pump-probe" spectroscopy that uses short pulses of light to excite the sample, adding rich information on the evolution of molecular states with time.

There are many forms of transient absorption spectroscopy, which use light pulses that may be anywhere from microseconds to attoseconds (1×10^{-15} s). Shorter pulses allow for

the experimenter to observe shorter time-scale physical processes. An example transient absorption experiment might consist of a set up similar to a UV-VIS spectrometer, with the addition of a pulsed excitation laser. The excitation laser, or pump beam, excites the sample with a high-energy pulse. A probe beam measures the transmission of the sample in the same area (but at a different angle to the pump), and in the same fashion as a UV-VIS spectrometer. The detector is electronically triggered by the excitation laser such that its signal as a function of time is referenced to the start of the pulse. A transient absorption measurement will build up a set of data that consists of a series of UV-VIS absorption measurements, each associated with a time (relative to the excitation pulse).

Transient absorption spectroscopy can reveal information about the transfer of energy within a molecule, or even a network of molecules, as a result of the excitation pulse. As an example with great relevance for this thesis, transient absorption has been used to observe the creation of photoexcited triplet states and photochemical products, as well as their decay with time [2].

2.4 Electron paramagnetic resonance

One of the primary techniques for measuring the spin states of samples is electron paramagnetic resonance (EPR), or electron spin resonance (ESR) spectroscopy. As discussed in section 1.1.4, the energy difference between spin levels is influenced by several intrinsic and extrinsic factors. EPR can probe these energy differences by measuring the microwave absorption of the sample. For experimental reasons, the sample absorption is measured at a fixed microwave frequency, and an external magnetic field is used to split the spin levels based on the Zeeman interaction. The locations and lineshapes of the various peaks measured by EPR spectroscopy can give the experimenter insights into the sample and its nanoscale local environment.

2.5 Optically-detected magnetic resonance

EPR spectroscopy is a quite general technique for observing the spin properties of a sample. However, one of its challenges is detecting the minuscule microwave absorption signal. Optically-detected magnetic resonance spectroscopy is able to perform spin measurements with much higher sensitivity than EPR by both polarizing, and reading out the spin signals using optical photons. This is only possible in systems that have coupled electronic and spin states. However, this requirement is not so uncommon. If we refer back to figure 1.1, we see that the spin-bearing triplet state T_1 is populated by ISC from the S_1 state, and then relaxes back to the ground S_0 state by phosphorescence. Both of these transition mechanisms are spin-dependent, and, therefore, create an avenue for optically-detected magnetic resonance of the triplet spin states.

CHAPTER 3

FLUORESCENT PROTEINS

Fluorescent proteins are one of the most successful biological research tools. They are a family of proteins that consists of a beta-barrel cage surrounding a central organic fluorophore that is formed by an autocatalytic reaction of neighboring amino acids [4]. This formation reaction typically takes place on the scale of minutes to hours. The structure of the enhanced yellow fluorescent protein, EYFP, is shown in figure 3.1. The organic fluorophore within the beta barrel, shown in figure 3.2, possesses an optical absorption associated with an excitation from its ground to excited singlet state, which then emits stokes-shifted fluorescence, as outlined in figure 1.1. The presence of this fluorescence emission in a small, stable, genetically-encodable protein is what makes fluorescent proteins the workhorse tool for labeling and sensing biological processes *in vivo*.

3.1 Photophysics

The original wild-type green fluorescent protein (wtGFP, or avGFP) was isolated from the jellyfish *Aequorea Victoria*. Shortly after its isolation, efforts began to better understand GFP's photophysics. Early studies revealed the presence of multiple ground states of the chromophore. One ground state is associated with a protonated (neutral), and another with a de-protonated (anionic) chromophore [5]. The neutral form possess an absorption peak at $\sim 400\,\text{nm}$, and the anionic at $\sim 480\,\text{nm}$, with its emission peak at $\sim 510\,\text{nm}$. Exciting the neutral chromophore results in an excited-state proton transfer that produces the anionic form, which then emits stokes-shifted fluorescence at $510\,\text{nm}$ [6].

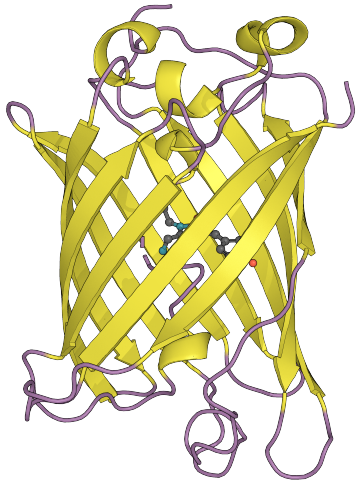


Figure 3.1: Structure of EYFP [3].

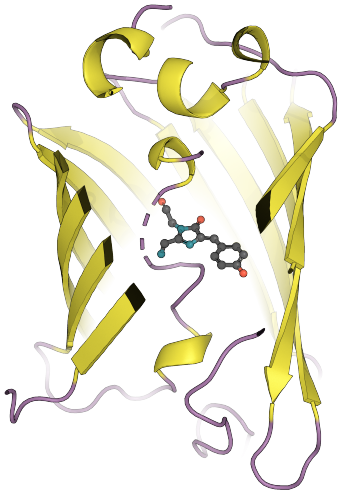


Figure 3.2: Structure of EYFP chromophore [3].

3.2 Directed evolution

Protein engineering efforts to improve the photophysical properties of avGFP also followed shortly after its isolation. Most new fluorescent protein variants were developed using directed evolution, a high-throughput technique that mimics evolution. It mutates a target gene to create many variants, but, unlike natural evolution, desirable variants are selected by the researcher. Repeating this mutation and selection process many times can result in a protein variant with improved properties, as dictated by the selection criteria. Since each amino acid in the target protein can be swapped for any other of the ∼20 remaining amino acids, there is an astronomically large search space of potential changes. Therefore, the key to success is reducing the size of the search space by identifying amino acid locations that are critical to the protein function, and screening as many variants as possible. The experimental technique for selecting desirable variants from a large library is typically the bottleneck in these methods, so it must be considered carefully to maximize the size of the library that can be searched.

Over the past decades, a vast library of different fluorescent protein variants has been

developed [7]. The enhanced green fluorescent protein (EGFP) stabilizes the anionic state of the chromophore, and has enhanced brightness compared to avGFP [8]. Enhanced yellow fluorescent protein (EYFP) has a slightly red-shifted absorption and emission. There are also other organisms with unique fluorescent proteins that have been identified and engineered to have blue- and red-shifted absorption and emission spectra, such as DsRed, [9]. Variants of fluorescent proteins have also been developed for sensing various biologically-relevant quantities, such as pH [10] or Ca ions [11].

3.3 Metastable triplet state

Metastable triplet states (T_1 shown in figure 1.1) are ubiquitous in conjugated organic fluorophores, like the one core to fluorescent proteins. The first conclusive evidence of the metastable triplet in fluorescent proteins was presented by Byrdin et al. in 2017 [2]. Its phosphorescence and transient absorption spectra were measured, and revealed its surprisingly long triplet lifetime of $\sim 3\,\text{ms}$.

3.4 Optically-activated delayed fluorescence

In section 1.4, we discussed fluorescence and phosphorescence as two potential photoluminescence mechanisms. Delayed fluorescence is another fairly common mechanism, which shares some properties of each. Like phosphorescence, it takes place on longer timescales. However, the transition responsible for its emission is a transition that emits fluorescence. The "delayed" nature of the fluorescence is usually due to the molecule becoming trapped in a long-lived dark state following photoexcitation. Eventually, the molecule may transition back to the excited singlet state and emit fluorescence. Sometimes, the transition back to the excited singlet state is thermally driven, and, thus, is termed thermally-activated delayed fluorescence.

Another mechanism that results in delayed fluorescence is a slightly more complicated process. It involves excitation from the metastable triplet dark state to a higher-excited triplet state. Then, intersystem crossing takes place from this higher triplet back to the singlet manifold. Finally, a delayed fluorescence photon is emitted from the excited singlet state. The measurement of this "optically-activated delayed fluorescence" (OADF) effect was pioneered in the Dickson lab, and has been measured on fluorescent proteins [12].

CHAPTER 4

OPTICS

Spectroscopic explorations often require customized optical microscopy systems. This chapter will introduce some basic concepts that may be useful for those building custom optical systems.

There are different levels of detail with which we can analyze the behavior of light. Generally, more accurate descriptions are more complex and mathematically cumbersome. Therefore, it is best to use the simplest possible model for the situation (but no simpler). Let's start by thinking about light as an electromagnetic field with an amplitude that varies throughout three-dimensional space, and time.

An extremely useful trick when dealing with electromagnetic waves is to treat them in the frequency (or Fourier) domain as a sum of sinusoids. The reason this is convenient is that the interaction of waves with linear, time-invariant systems can be described with simpler mathematics in the frequency domain than the time domain. And many things are quite linear and time invariant. Therefore, going forward, we will consider electromagnetic fields as waves that vary sinusoidally with space and time, since a more complex field can be decomposed into these simpler waves using a Fourier transform. A sinusoidal electromagnetic field has a frequency, which dictates how fast it oscillates with time, an amplitude that determines its strength, and a phase offset, which encodes the position within the cycle of the sinusoid. In vacuum, light travels at a fixed velocity, c. However, when light travels through a medium (not vacuum), its speed is slowed by a factor of n, the "index of refraction" of the medium. The index of refraction is an important optical property of materials, and dictates how light interacts with the material, as we will see shortly. Since the speed of a wave is related to its wavelength and frequency by $\nu = f\lambda$, we can write an equivalent equation for a light wave: $\frac{c}{n} = f\lambda$.

Broadly speaking, when electromagnetic waves interact with an object, their behavior

can be categorized into "near-field" and "far-field" regimes. Near-field behavior takes places at distances to the object on the order of, or shorter than, the wavelength, whereas far-field behavior takes place at distances somewhat longer than the wavelength. Here, we will primarily consider "far-field" behavior.

4.1 Polarization

In addition to the properties discussed above, a light wave also possesses a polarization, which indicates the direction of its electric field vector relative to the wave propagation direction. A material's index of refraction, as well reflection off of surfaces can depend on the polarization of the light. If a material has a polarization-dependent index of refraction, it is birefringent. This property can be utilized to manipulate the polarization of incoming light, and create so-called half- or quarter-wave plates. When light impinges on a surface, its reflection depends on the polarization of the light, as we will see in the next section. The plane formed by the surface normal and propagation direction of the light is the plane of incidence. If light is polarized parallel with this plane of incidence, it is p-polarized, whereas if it is polarized perpendicular to the plane of incidence it is s-polarized.

4.2 Reflection & refraction

Let's now build up some simple relations that help to explain the behavior of light rays. If a ray is traveling through a medium with index of refraction n_i, and it impinges on an interface with a second medium with index n_t, it can either reflect off of the interface, enter the second medium, or a bit of both. The portion of the light beam that enters the second medium "refracts" at the interface, changing direction according to Snell's Law

$$n_i \sin(\theta_i) = n_t \sin(\theta_t), \tag{4.1}$$

where θ_i is the angle between the incident ray and the vector normal to the interface, and θ_t is the same for the transmitted (refracted) ray. We can use the Fresnel equations to predict the amount of light that will be reflected at the interface, according to

$$R_s = \left[\frac{n_t \cos(\theta_i) - n_i \cos(\theta_t)}{n_t \cos(\theta_i) + n_i \cos(\theta_t)}\right]^2 R_p = \left[\frac{n_t \cos(\theta_t) - n_i \cos(\theta_i)}{n_t \cos(\theta_t) + n_i \cos(\theta_i)}\right]^2, \tag{4.2}$$

where R_s is the reflected power fraction for s-polarized light, and R_p for p-polarized light. The unreflected light is transmitted (refracted), so $T_s = 1 - R_s$ and $T_p = 1 - R_p$, where T_s and T_p represent the transmitted power for s- and p-polarized light, respectively.

There are a few interesting features of Snell's law that should be noted. If $n_t > n_i$, the light refracts such that it's angle with the interface normal gets smaller. If $n_i > n_t$, the light refracts away from the interface normal. Therefore, the ray always bends towards the material with higher index. If $n_i > n_t$ and

$$\theta_i >= \arcsin(\frac{n_t}{n_i}), \tag{4.3}$$

Snell's law breaks down. In this situation, the ray will undergo "total internal reflection", where it is completely reflected off of the interface. This is the basis for fiber optical cables. An interesting consequence of total internal reflection worth mentioning is what happens near the interface. A full description requires a more complex near-field wave analysis of the light impinging on the interface, which is beyond the scope of this chapter. However, suffice it to say, that a small amount of light at the interface "leaks" into the other medium, but, importantly, it does not propagate into that medium. It's intensity decays exponentially with distance from the interface with a characteristic length scale comparable to the light wavelength. This is the basis of total internal reflection fluorescence microscopy.

4.3 Ray optics

Ray optics is a highly simplified, but surprisingly powerful framework for designing optical systems. Instead of representing light as a wave, it is considered to be a bundles of rays, where each ray is a vector that represents the propagation direction of the light.

4.3.1 Paraxial approximation

In many optical systems, there is rotational symmetry about an "optical axis". If a light ray is traveling through an optical system and it impinges on an interface between two materials with different indices of refraction, it will undergo refraction according to Snell's law as discussed previously. In the case that the light ray has a small angle to the optical axis, θ_i and θ_t are small and we can make the assumption that

$$\sin(\theta_i) \approx \theta_i, \text{ and}$$

$$\sin(\theta_t) \approx \theta_t, \text{ so}$$

$$n_i\theta_i \approx n_t\theta_t. \tag{4.4}$$

This is termed the "paraxial approximation", and is quite useful because it linearizes Snell's law. In an optical system consisting of many components, figuring out how light propagates through the system is, in general, a complicated task, even when using ray optics (as opposed to a more complex wave treatment), and would be impractical to solve analytically. However, using the paraxial approximation, we can convert this problem into a simple exercise in solving algebraic equations. Of course, a real optical system must deal with the errors introduced by the paraxial approximation. However, design practices to correct for, or minimize, these errors (aberrations) tend to do so such that the optical system matches what is predicted by the paraxial approximation.

4.4 Ray-transfer matrices

A convenient way of solving for the basic optical properties of a system is by tracing the path of a few rays through the system. Using the paraxial approximation, we can write down some simple expressions to perform this ray tracing. We let the ray be represented by a vector $\left[\begin{smallmatrix} x \\ \theta \end{smallmatrix}\right]$, where x is the lateral distance of the ray from the optical axis, and θ is its angle to the optical axis. If the light ray is traveling through a medium with constant index, its position, x, will change, but its angle, θ, will remain constant. Let's assume the medium has a thickness, t. Then, the new lateral position of the ray, x' after propagating through the medium will be given by $x' = x + t\tan(\theta) \approx x + t\theta$. We can write this in matrix form as

$$\begin{bmatrix} x' \\ \theta' \end{bmatrix} = R \begin{bmatrix} x \\ \theta \end{bmatrix} = \begin{bmatrix} 1 & t \\ 0 & 1 \end{bmatrix} \begin{bmatrix} x \\ \theta \end{bmatrix}, \tag{4.5}$$

where R is the ray-transfer matrix. Now, let's imagine the ray impinges on an interface with another medium. x will not change when the ray strikes the interface, but θ will be modified according to Snell's law: $n\theta = n'\theta'$. Again, we can write down a ray-transfer matrix to represent this scenario

$$\begin{bmatrix} x' \\ \theta' \end{bmatrix} = \begin{bmatrix} 1 & 0 \\ 0 & \frac{n}{n'} \end{bmatrix} \begin{bmatrix} x \\ \theta \end{bmatrix}. \tag{4.6}$$

We can also generate a combined matrix that represents each of these operations happening in sequence

$$\begin{bmatrix} x' \\ \theta' \end{bmatrix} = \begin{bmatrix} 1 & 0 \\ 0 & \frac{n}{n'} \end{bmatrix} \begin{bmatrix} 1 & t \\ 0 & 1 \end{bmatrix} \begin{bmatrix} x \\ \theta \end{bmatrix} = \begin{bmatrix} 1 & t \\ 0 & \frac{n}{n'} \end{bmatrix} \begin{bmatrix} x \\ \theta \end{bmatrix}. \tag{4.7}$$

4.5 Basic optical components

4.5.1 Lenses

A lens is an optical component that is shaped to take advantage of the refraction of light on its surfaces. The most common lenses have spherical surfaces because they are easier to manufacture. More complex aspheric lenses can also be used in order to minimize aberrations. When a beam of collimated light ($\theta = 0$) enters a lens, it will either converge to a focus, or diverge. The focal length of a lens is defined as the distance along the optical axis from the lens to the location at which the light converges to a common point. It can be calculated by tracing a ray through the lens surfaces. For example, let's assume a lens with a radius-of-curvature of R_1 on its first surface, R_2 on its second surface, and made of glass with an index of n_g. The ray-transfer matrix for refraction at a curved surface is given by

$$\begin{bmatrix} x' \\ \theta' \end{bmatrix} = \begin{bmatrix} 1 & 0 \\ \frac{n-n'}{Rn'} & \frac{n}{n'} \end{bmatrix} \begin{bmatrix} x \\ \theta \end{bmatrix}, \tag{4.8}$$

where R is the radius-of-curvature of the surface, n is the initial index, and n' is the final index. We will also assume this is a "thin lens", such that the lens thickness is negligible compared to the other distances, and that the lens is immersed in air ($n = 1$). Now, we can solve for the focal length by setting the final lateral position $x' = 0$ and letting the light propagate a distance f after the lens:

$$
\begin{aligned}
\begin{bmatrix} 0 \\ \theta' \end{bmatrix} &= \begin{bmatrix} 1 & f \\ 0 & 1 \end{bmatrix} \begin{bmatrix} 1 & 0 \\ \frac{n_g-1}{R_2} & n_g \end{bmatrix} \begin{bmatrix} 1 & 0 \\ \frac{1-n_g}{R_1 n_g} & \frac{1}{n_g} \end{bmatrix} \begin{bmatrix} x \\ 0 \end{bmatrix} \\
&= \begin{bmatrix} 1 & f \\ 0 & 1 \end{bmatrix} \begin{bmatrix} 1 & 0 \\ \frac{n_g-1}{R_2} & n_g \end{bmatrix} \begin{bmatrix} x \\ x(\frac{1-n_g}{R_1 n_g}) \end{bmatrix} \\
&= x \begin{bmatrix} 1 & f \\ 0 & 1 \end{bmatrix} \begin{bmatrix} 1 \\ \frac{n_g-1}{R_2} + n_g \frac{1-n_g}{R_1 n_g} \end{bmatrix} \\
&= x \begin{bmatrix} 1 + f(\frac{n_g-1}{R_2} + \frac{n_g-1}{R_1}) \\ \frac{n_g-1}{R_2} - \frac{n_g-1}{R_1} \end{bmatrix} \\
0 &= 1 + f(n_g - 1)(\frac{1}{R_2} - \frac{1}{R_1}) \\
\frac{1}{f} &= (n_g - 1)(\frac{1}{R_1} - \frac{1}{R_2}).
\end{aligned}
\tag{4.9}
$$

This is known as the lensmaker's formula. Calculating the formula for a thick lens is just a matter of adding an additional ray-transfer matrix between the two curved surfaces. We can also treat a generic thin lens as a ray-transfer matrix without worrying about the curvature of its surfaces:

$$
\begin{bmatrix} x' \\ \theta' \end{bmatrix} = \begin{bmatrix} 1 & 0 \\ -\frac{1}{f} & 1 \end{bmatrix} \begin{bmatrix} x \\ \theta \end{bmatrix}. \tag{4.10}
$$

4.5.2 Mirrors

Mirrors are probably familiar to the reader, but it should be noted that mirrors can also be made to converge and diverge light. Mirrors with spherical surfaces behave somewhat like lenses, except that they can be more difficult to use since light that they reflect will be coming right back towards the source. A particularly handy type of mirror is an off-axis parabolic mirror. This special mirror can collimate a point source at a 45° angle and vice

versa. However, unlike a lens, the light will only be collimated if the point source is exactly at the focus of the parabola, which makes it somewhat more difficult to align.

4.5.3 Dichroic mirrors & filters

Filters and mirrors with low-, high-, and band-pass spectral responses can be designed by the use special dielectric coatings. These components are critical to spectroscopy, and enable the high-fidelity separation of different light wavelengths. This is quite important, for example, in fluorescence microscopy for filtering out the excitation light reflected off the sample, which would otherwise overwhelm the fluorescence signal.

4.6 Beam expander

Let's imagine we have two lenses with focal lengths f_1 and f_2. If we place the lenses a distance $f_1 + f_2$ apart, we have a special system called a beam expander. We can analyze its behavior using ray-transfer matrices:

$$\begin{aligned}
\begin{bmatrix} x' \\ \theta' \end{bmatrix} &= \begin{bmatrix} 1 & 0 \\ -\frac{1}{f_2} & 1 \end{bmatrix} \begin{bmatrix} 1 & f_1+f_2 \\ 0 & 1 \end{bmatrix} \begin{bmatrix} 1 & 0 \\ -\frac{1}{f_1} & 1 \end{bmatrix} \begin{bmatrix} x \\ \theta \end{bmatrix} \\
&= \begin{bmatrix} 1 & 0 \\ -\frac{1}{f_2} & 1 \end{bmatrix} \begin{bmatrix} 1-\frac{f_1+f_2}{f_1} & f_1+f_2 \\ -\frac{1}{f1} & 1 \end{bmatrix} \begin{bmatrix} x \\ \theta \end{bmatrix} \\
&= \begin{bmatrix} 1-\frac{f_1+f_2}{f_1} & f_1+f_2 \\ -\frac{1}{f_2}+\frac{f_1+f_2}{f_1 f_2}-\frac{1}{f_1} & -\frac{f_1+f_2}{f_2}+1 \end{bmatrix} \begin{bmatrix} x \\ \theta \end{bmatrix} \\
&= \begin{bmatrix} -\frac{f_2}{f_1} & f_1+f_2 \\ 0 & -\frac{f_1}{f_2} \end{bmatrix} \begin{bmatrix} x \\ \theta \end{bmatrix}.
\end{aligned} \tag{4.11}$$

If we let the input light have $\theta = 0$ (collimated light), we can see that the output is also collimated, but its beam diameter has been changed by a factor of $-\frac{f_2}{f_1}$. Thus, we have

created a way to expand (or contract) an optical beam.

4.7 Microscope

Now let's take the beam expander from the last example, and add some distance for the light to propagate before and after the optical system. We will add a distance f_1 before, and f_2 after. We find that

$$\begin{aligned}
\begin{bmatrix} x' \\ \theta' \end{bmatrix} &= \begin{bmatrix} 1 & f_2 \\ 0 & 1 \end{bmatrix} \begin{bmatrix} -\frac{f_2}{f_1} & f_1 + f_2 \\ 0 & -\frac{f_1}{f_2} \end{bmatrix} \begin{bmatrix} 1 & f_1 \\ 0 & 1 \end{bmatrix} \begin{bmatrix} x \\ \theta \end{bmatrix}, \\
\begin{bmatrix} x' \\ \theta' \end{bmatrix} &= \begin{bmatrix} -\frac{f_2}{f_1} & 0 \\ 0 & -\frac{f_1}{f_2} \end{bmatrix}, \\
x' &= -\frac{f_2}{f_1} x, \\
\theta' &= -\frac{f_1}{f_2} \theta,
\end{aligned} \tag{4.12}$$

As you can see, x (and θ) are simply multiplied by a factor given by the ratio of the focal lengths. $f_2/f_1 = M$ is the magnification of the system. Every point on the initial plane is "imaged" onto a corresponding point on the "focal" plane. The image is flipped compared to the original (due to the negative sign). By choosing the magnification $M > 1$, we can look at objects that are smaller than what we can see with the naked eye. This is the basis of microscopy.

4.8 Aberrations

Optical aberrations are the deviation of behavior in an optical system from that predicted by the paraxial approximation. There are many different types of aberrations. We will only discuss a few here.

4.8.1 Spherical

Spherical aberration is a variation in the focal point of an optical system as a function of the distance from the optical axis. As discussed in section 4.3.1, the behavior of real lenses departs from that predicted by the paraxial approximation due to the difference between θ and $\sin(\theta)$. However, spherical aberration can be corrected relatively easily by using an aspheric lens, which departs from a spherical surface in a way that cancels the $\sin(\theta)$ error. However, with a single aspheric surface, this correction is only valid for a single point and light wavelength.

4.8.2 Chromatic

Chromatic aberration is a variation in the focal point of an optical system as a function of the light wavelength. Chromatic aberrations are a product of the variation in the index of refraction of materials with wavelength, or *dispersion*. Using pairs of lenses made of different materials, with different dispersions, can allow for the partial cancellation of chromatic aberration. A commonly encountered optical element is an "achromatic doublet", which is two such lenses with one surface having a common radius of curvature, where the lenses have been cemented together. While these lenses have better chromatic performance than a single-material lens, the chromatic aberration is only corrected at two wavelengths.

CHAPTER 5

EXPERIMENTAL HARDWARE

The majority of the measurements in this work were performed on a custom-built scanning confocal microscope. The system was designed and optimized for performing pulsed optically-detected magnetic resonance spectroscopy at cryogenic temperatures, as opposed to imaging, which is the more common purpose of a confocal microscope. Many aspects of the measurements were automated, which greatly simplifies the collection of experimental data. I highly recommend future experimentalists to automate their systems. In addition to simplifying data collection, it also reduces the risk of user errors, which can become problematic in complex experiments with a lot of disparate components.

5.1 Mechanics

5.1.1 Cryogenics

In order to measure a molecules' spin properties using standard optical-detection techniques, its spin-lattice relaxation time (T_1) must be sufficiently long. The relaxation rate ($1/T_1$) typically scales strongly with temperature, so it is often favorable to operate at lower temperatures in order to prolong the spin T_1.

Since the spin properties of EYFP were unknown before the experiments described in chapter 8, the most cautious approach was to take measurements at very low temperatures. Therefore, the microscope was built to probe samples within a closed-cycle helium cryostat from Montana Instruments. The cryostat components primarily operate at three different temperatures: room temperature, 30 K, and a programmable sample temperature, which can go down to 4 K. The "vaccuum shroud" of the cryostat is at room temperature and creates an air-tight seal around the other components. The "heat shield" usually operates at 30 K, and encloses the cold finger where the sample is mounted, which can be as low as 4 K.

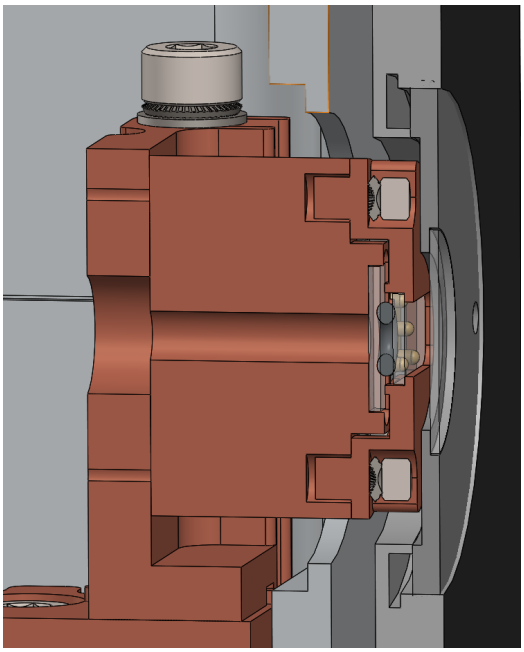


Figure 5.1: Cryogenic sample mount CAD model side cross-sectional view.

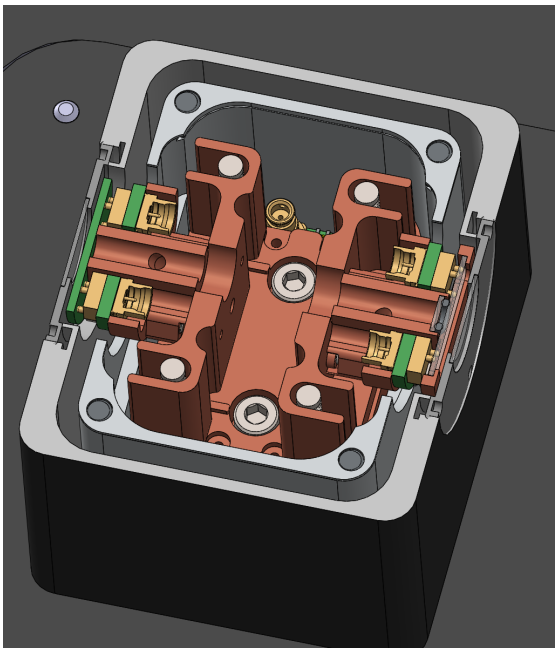


Figure 5.2: Cryogenic sample mount CAD model top cross-sectional view.

The interior of the cryostat must be under vaccuum in order to minimize heat conduction from the vaccuum shroud to the heat shield and cold finger. At liquid-helium temperatures, blackbody radiation must also be taken into account. Thermal radiation emitted from the vaccuum shroud and absorbed by the cold finger would produce an unacceptably large source of heat. Therefore, the heat shield at 30 K surrounds the cold finger, drastically reducing the impact of blackbody radiation. The microscope uses an "out-of-cryo" objective, which operates at ambient conditions outside of the vaccuum shroud. In order to maximize the collection efficiency of emission from the sample and achieve small excitation laser spot sizes, an objective with a high numerical aperture is used. These objectives typically have millimeter-scale working distances, so the sample must be very close to the glass window in the vaccuum shroud that gives optical access to the sample.

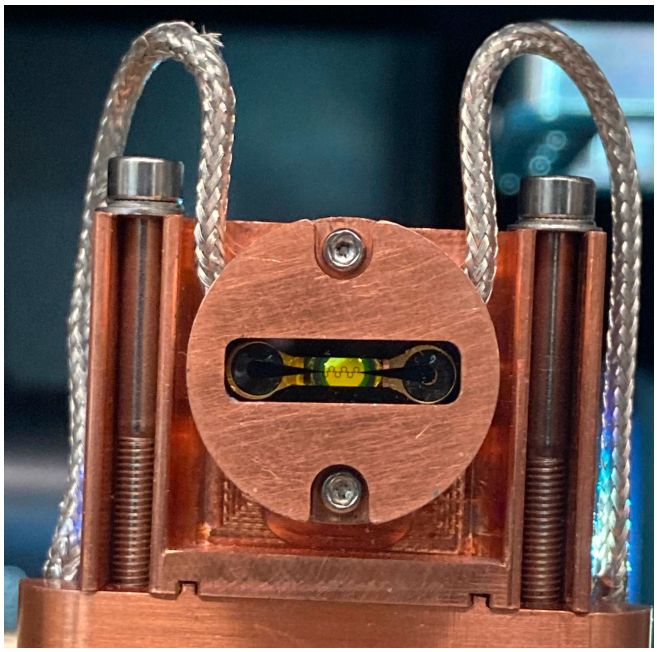


Figure 5.3: Cryogenic sample mount containing aqueous EYFP.

5.1.2 Sample mount

A computer-aided design (CAD) model of the sample holder and heat shield that we designed for our experiments is shown in figures 5.1 and 5.2. The actual fabricated sample holder is shown in figure 5.3. The sample is enclosed in a $\sim 5\,\mu L$ liquid cell, which consists of two pieces of sapphire and a silicone o-ring. The sealed liquid cell maintains the sample at standard atmospheric pressure while the rest of the cryostat is held under vaccuum, which prevents the aqueous sample from boiling in the low-pressure conditions. Sapphire is used to enclose the sample, since it is optically transparent and has high thermal conductivity at low temperatures.

5.1.3 Sample coverslip

The sapphire piece closest to the sample, the "coverslip", is lithographically patterned with a microwave structure that excites the spin transitions in the sample. The pattern (figure 5.4) was designed using gdstk and then fabricated in a cleanroom using a standard lift-off

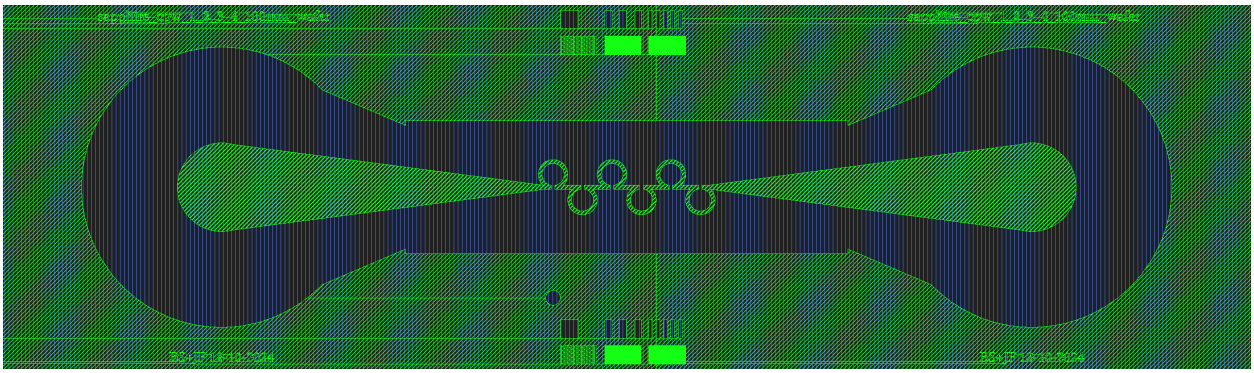


Figure 5.4: Lithographic pattern for coverslip microwave drive structure.

process with AZ nLOF 2070 photoresist. The metal coating consists of a thin Cr adhesion layer, $\sim 2\,\mu m$ of Cu, and a 100 nm Au capping layer. Landing pads on either side of the pattern mate with spring-loaded contacts (Rosenberger 99CI106-030L5) from the sample mount. The sample was primarily measured inside of the omega-shaped structures.

5.2 Optics

5.2.1 Lasers

For simplicity, low-cost Fabry-Perot diode lasers were used to excite the sample. The laser power is controlled with a set of neutral-density filters (some in an automated filter wheel), as well as by changing the drive current of the laser diode driver.

5.2.2 Acousto-optic modulators

In order to generate light pulses, the lasers were gated with acousto-optic modulators (AOM). Another AOM is used to gate the PL signal received by the detector. AOMs have relatively high temporal resolution ($< 100\,ns$), which is useful in separating small optical signals from other large emission signals that occur in close temporal proximity.

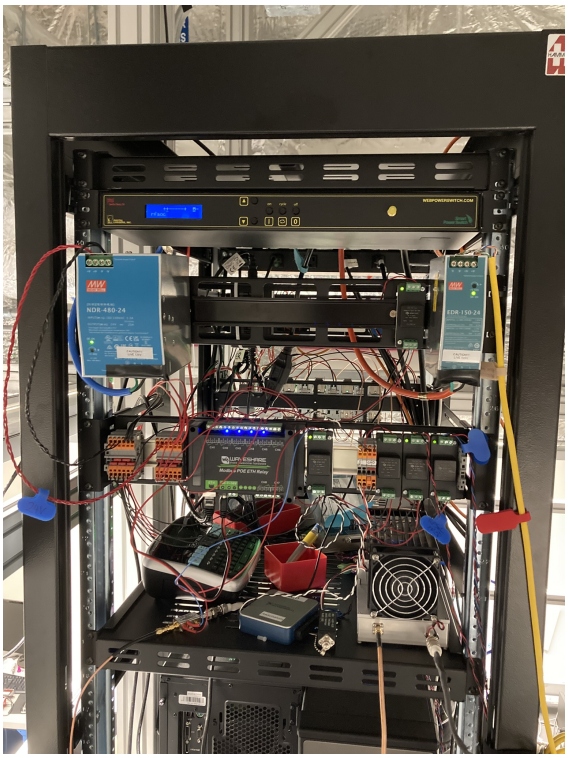


Figure 5.5: Server rack (front).

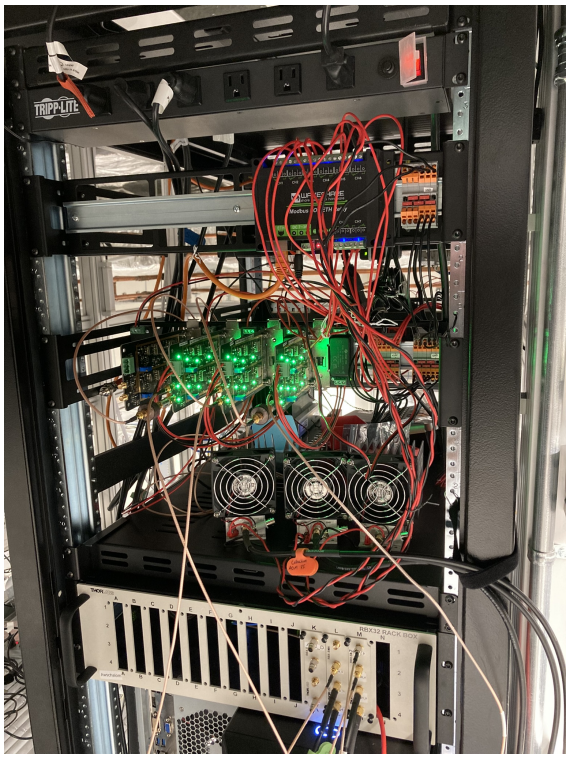


Figure 5.6: Server rack (back).

5.2.3 Detectors

The primary detector used in the measurements was a single-photon counting module (SPCM, Excelitas SPCM-AQRH-14) based on an avalanche photodiode (APD). The APD is operated in "geiger mode" such that a single photon impinging on the photosensitive area of the APD can cause an avalanche effect that builds up a large current spike that is easily detected by conventional electronics. Measurements of emission spectra were taken with a Princeton Instruments Acton SpectraPro 2500i spectrometer.

5.3 Electronics

In addition to the lasers and detectors, many other electronic components are required to run the experiment. The "brains" of the operation is an experimental pulse generation and processing system called QICK [13, 14], based on the RFSoC by AMD/Xilinx. A

customized version of QICK was used to synthesize the microsecond-scale coordinated digital and microwave pulses that define the sequence to run a specific experiment, and is described in greater detail in chapter 6. Data from the SPCM photon detector can be collected and processed by QICK, however, this capability was not completed at the time of the experiments in this work, so an external time-tagger made by Swabian Instruments was used. Microwave pulses generated by the RFSoC are fed into a power amplifier before entering the cryostat. Custom circuit boards were designed for driving the AOMs in order to minimize power fluctuations in the light transmitted through the AOMs that could be confused for time-dependent signals coming from the sample. In retrospect, these custom AOM drivers were likely unnecessary since the optically-detected spin contrast is high, however, they may be useful for measuring other small-contrast time-dependent PL signals.

A convenient way of mounting and wiring all of these electronic components is a server rack. A server rack is essentially a cabinet with a set of standardized mounting holes that the instruments can be slotted into. Instruments that do not have rack-mounting hardware can be placed on rack-mount shelves. Figures 5.5 and 5.6 show the server rack used to house the electronics used for the experiments.

5.3.1 Power distribution

In an experimental system such as the one detailed here, there can be many instruments that require power. Automating the process of turning these instruments on and off (as well as configuring the instruments) can be quite helpful when they may also have complex sets of dependencies for a given experiment.

Controlling the power state of instruments that require AC power was accomplished with an ethernet-controlled rack-mount power strip (Digital Loggers 222). Similarly, DC-powered instruments were controlled with a ethernet-controlled relay module (Waveshare 24964). A rack-mounted DIN rail (Hammond RMAD19003BK) is a convenient way of mounting the

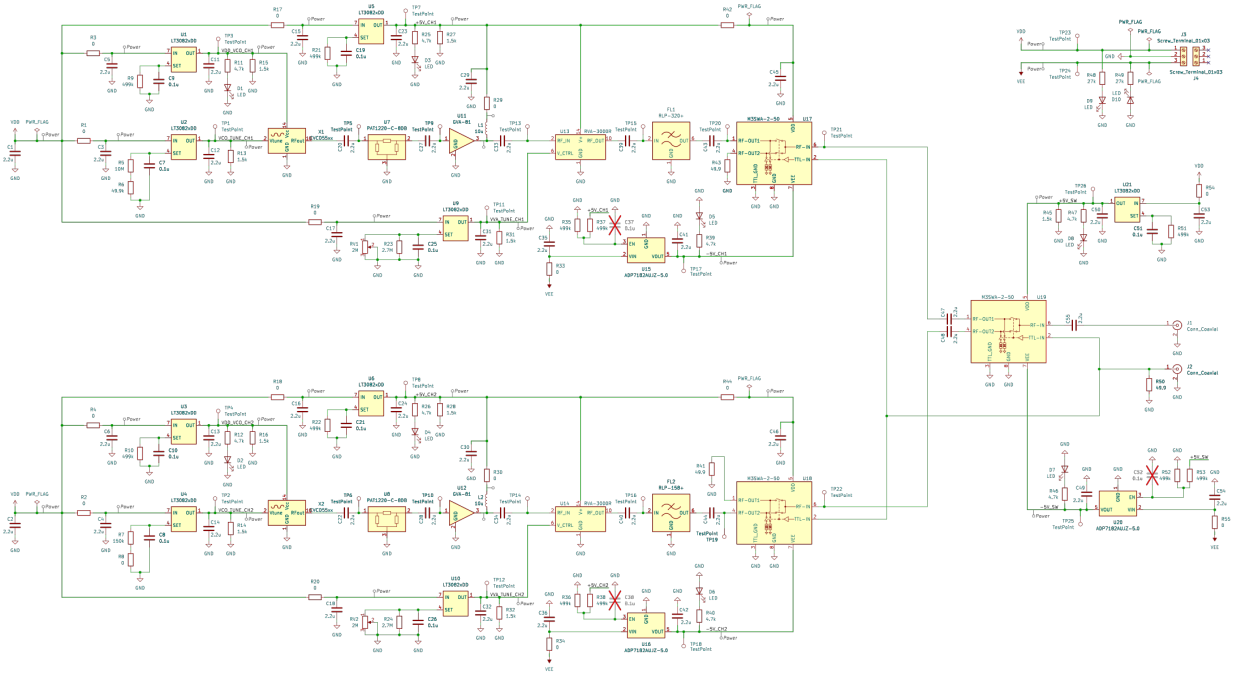


Figure 5.7: 2-tone AOM driver schematic.

small DC-DC power supplies.

Instruments that required AC power were simply plugged into the rack-mount power strip. Instruments requiring DC power were controlled with the ethernet-controlled relay module. An AC-DC power supply was used to generate a 24 VDC supply, which fed downstream supplies. Each instrument requiring its own separately-controlled supply had an associated low-cost DC-DC DIN-mounted power supply. This supply was fed from the 24 VDC supply, and wired to the ethernet-controlled relay module, such that switching on the relay then delivered power to the downstream instrument. The wiring was performed with DIN-mount terminal blocks.

5.3.2 AOM driver PCB

When generating light pulses with an AOM, two parameters that may be important are the isolation and power stability. The isolation (usually expressed in dB) is defined as $10\log_{10}(P_{\text{on}}/P_{\text{off}})$, where P_{on} is the transmitted optical power with the AOM enabled, and



Figure 5.8: 2-tone AOM driver PCB.

P_{off} is the transmitted optical power with the AOM disabled. A low isolation means that even when the AOM is disabled, there is significant light leakage through the AOM, which can be undesirable for certain applications.

Power stability is the change in transmitted optical power as a function of time or AOM duty cycle. The active area of an AOM that the optical beam passes through is made of a material whose optical index of refraction changes with strain (acoustic waves), producing the desired beam diffraction. However, other variables, such as temperature, can impact the index of refraction and, therefore, the pointing stability of the beam.

Traditional AOM drivers produces a single tone, which is toggled on and off, often with relatively RF low isolation. Therefore, the optical power is switched between being primarily concentrated in the 0th order diffraction peak (AOM disabled, RF off) and the 1st order peak (AOM enabled, RF on). This approach produces two undesirable effects. First, drivers with low isolation (RF power $P_{\text{on}}/P_{\text{off}}$) can limit the optical isolation of the AOM due to parasitic driving of the AOM with RF leakage. Second, when switching the RF drive on/off, there is a change in RF power dissipation in the AOM crystal, inducing a temperature change. This

temperature change reduces the beam pointing stability and produces power fluctuations as a function of time and switching duty cycle.

The custom 2-Tone AOM driver designed for this experiment greatly reduces isolation and power stability issues. Rather than switching an RF signal on or off, this driver switches between two different RF frequencies. The optical power diffracted by the AOM with lower-frequency RF drive is fiber coupled into a single-mode fiber and then sent to the experiment. The optical power diffracted by the AOM with the higher-frequency ("dummy") drive is directed into a beam-dump. The power at the two frequencies produced by the driver are calibrated such that thermalization effects of the AOM crystal are minimized, since the RF power delivered to the crystal is equal for both frequencies. The driver can switch between these two frequencies with very high RF isolation such that the achievable AOM optical isolation will likely become limited by the physics of gaussian optics (see additional discussion below).

A schematic of the circuit is shown in figure 5.7, and the assembled PCB in figure 5.8. The driver consists of four main parts: two nearly-identical frequency synthesis sections, a fast RF switch to select the frequency, and an (off board) RF amplifier. The frequency synthesis sections begin with a voltage-controlled oscillator that generates the initial RF signal (CVCO55xx). A fixed attenuator limits the maximum output power (PAT1220-C-x). Next, an amplifier increases the output power (GVA-81). A voltage-variable attenuator allows the user to tune the output power of each frequency synthesis channel in real-time using a potentiometer, in order to calibrate the system (RVA-3000R). A filter reduces some of the harmonics (RLP-xxx+). An RF switch (M3SWA-2-50DRB+) for each frequency synthesis channel toggles the frequency on/off before the final switch in order to increase isolation. This concludes the frequency synthesis sections. A final RF switch (M3SWA-2-50DRB+) selects the output frequency channel. The AOM driver output is intended to then be fed to an external RF amplifier (ZHL-03-5WF+).

5.3.3 Microwave electronics

The RFSoC can output $\sim 0\,\mathrm{dBm}$ from its microwave outputs. In order to drive fast Rabi oscillations ($< 50\,\mathrm{ns}$) between the spin triplet sublevels, $\sim 1\,\mathrm{W}$ must be delivered to the sample. Therefore, the RFSoC outputs are fed into a preamp, then a microwave power amplifier (Minicircuits ZHL-15W-422-S+).

CHAPTER 6

PULSE GENERATION

Most experimental pulse sequences used in this work take place on the micro and nanosecond time scale. Controlling, e.g. the AOMs that turn the lasers on and off, requires high-speed digital pulses, whereas driving the spin transitions in the sample requires microwave-frequency pulses. A traditional way of synthesizing these sets of coordinated digital and RF pulses is with a combination of hardware consisting of signal generators, microwave switches, and an arbitrary waveform generator. Advancements in integrated circuit design have enabled the proliferation of high-performance digital-to-analog (DAC) and analog-to-digital (ADC) converters that are able to directly synthesize/measure microwave frequencies, obviating the need for separate signal generators, mixers, and switches. Direct digital synthesis (DDS) of the microwave-frequency pulses also avoids issues such as mixer carrier feedthrough and other artifacts.

6.1 RFSoC

The radio-frequency system-on-a-chip (RFSoC) platform created by AMD/Xilinx contains an array of DACs and ADCs with giga-sample-per-second (GSPS) operation frequencies tightly integrated with field-programmable gate array (FPGA) logic, as well as an ARM microprocessor. This powerful system is ideal for the control and measurement of optically-addressable spin sensors. Development boards available from AMD/Xilinx and other suppliers provide a simple entry point for using the RFSoC. Many different boards are available, but here we will focus on the RFSoC 4×2 by RealDigital. This development board is a particularly promising platform because it provides enough inputs/outputs (IO) for the most commonly performed experiments, and is extremely low-cost with an academic discount that puts the final price at the time of writing at $2149, which is significantly cheaper than all of

the instruments required in a more traditional setup.

6.1.1 RF outputs

The RFSoC 4×2 has 2× DACs operating at up to 9.85 GSPS. Operation in the 2nd Nyquist zone of the DAC allows it to synthesize frequencies up to 9.85 GHz. While DDS of microwave signals comes with many advantages, it also creates some potential issues that must be considered. When synthesizing a frequency, f, the DAC also generates a tone at $f_s - f$, where f_s is the sample frequency. Therefore, operation in the region around $f_s/2$ is prone to interference from the nearby $f_s - f$ tone. Frequency planning is necessary in order to avoid such issues.

6.1.2 RF inputs

The RFSoC 4×2 has 4× ADCs operating at up to 5 GSPS. These inputs can be used to sample signals from analog detectors, such as photomultiplier tubes (PMTs), photodiodes (PDs), or avalanche photodiodes (APDs). They can also be used as inputs for time-tagging the output of an SPCM, as will be discussed later.

6.1.3 Digital outputs

The RFSoC 4×2 has many digital IOs that can be utilized as trigger signals. They are available in the form of PMOD or SYZYGY interfaces.

6.2 Quantum instrumentation control kit (QICK)

QICK is an open-source firmware/software package for the RFSoC hardware that turns it into a sophisticated pulse generation and processing platform [13, 14]. The firmware running on the FPGA programmable logic (PL) consists of two main components: a soft-



Figure 6.1: custom ADC and digital output buffer PCBs for interfacing the RFSoC 4×2 with common lab instrumentation.

core processor called the "tproc", which interprets the user's assembly-code programs, and the signal generation and timing logic.

The assembly code program defines the experimental pulse sequence. Special assembly instructions and registers within the tproc allow for the configuration and queueing of digital or RF pulses to be played. The tproc and signal generation logic are asynchronous, and are connected by first-in-first-out (FIFO) buffers. The tproc assembly instructions cannot play pulses directly, they only add commands to these FIFO pulse queues. The signal generation logic processes the items from the pulse queues, and attempts to synthesize and play the pulses at the requested times.

6.2.1 QICK-SPIN

The QICK platform was originally developed for superconducting qubit experiments. While there is a significant overlap in the control requirements for superconducting qubits and optically-addressable spin qubits, certain aspects of our experiments were not initially addressed by QICK, for example, the need for high-speed digital outputs to trigger lasers and detectors tightly integrated with the microwave pulses. The original QICK platform had the ability to play digital outputs, but they were internally interdependent, which made their use difficult. QICK-SPIN is a collaborative project with the developers of QICK to make it more friendly for measuring optically-addressable spin qubits. QICK-SPIN has fully independent digital channels, as well as a built-in time tagger. Furthermore, a set of custom hardware was designed in order enable interfacing of the RFSoC platform with instrumentation used in our experiments, as shown in figure 6.1.

6.2.2 Time tagger

QICK has integrated analog signal readout functionality that uses the RFSoC's high-performance ADCs, which is ideal for collecting data from detectors like PMTs or PDs. However, many optically-addressable spin qubit experiments utilize SPCMs for data collection, which output digital pulses. QICK-SPIN integrates a time-tagger firmware block that is able to detect the digital pulses generated by an SPCM, while being tightly integrated with the user program.

The time tagger is armed by the user program using an internal digital trigger pulse. On the rising edge of this ARM signal, the time tagger will begin tagging pulses from its ADC input. The arrival time of each pulse is registered relative to the time of the ARM pulse rising edge. The falling edge of the ARM signal indicates the end of a readout block, and disarms the time-tagging functionality. The time-tagger data is pushed into two FIFO buffers. The first buffer contains the number of time tags collected during each ARM pulse, and the second contains the time tag values. This allows each time tag to be correlated with



Figure 6.2: Custom RFSoC ADC input buffer PCB schematic.

the experiment in which it was collected.

6.2.3 RF input buffer PCB

The RFSoC platform is primarily intended for users generating and receiving microwave signals. Therefore, the RFSoC 4×2 development board RF inputs and outputs are AC coupled to the output connector using a balun. However, measurements that utilize the ADC to measure the outputs from optical detectors like PMTs or photodiodes may require a DC-coupled signal. While the RFSoC 4×2 was not designed for this purpose, it can be modified to accept DC-coupled inputs. First, single-ended signals coming from a detector



Figure 6.3: Custom RFSoC ADC input buffer PCB.

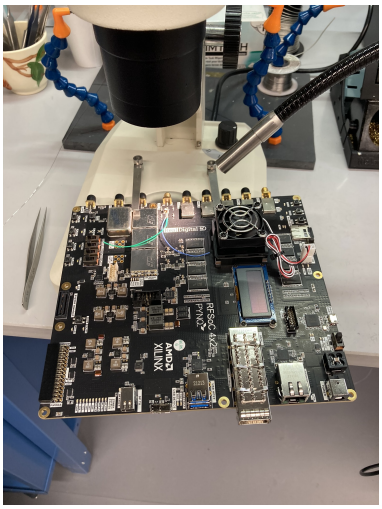


Figure 6.4: RFSoC ADC differential input wires soldered to C302 and C303 pads.

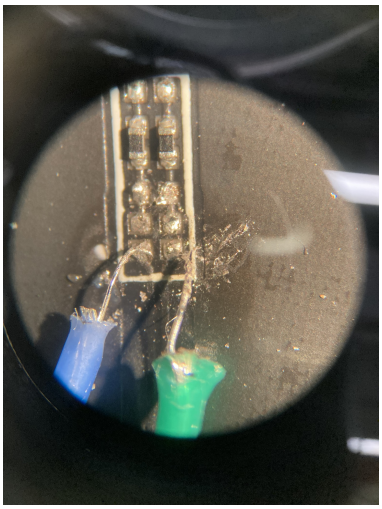


Figure 6.5: RFSoC ADC differential input wires soldered to C302 and C303 pads.

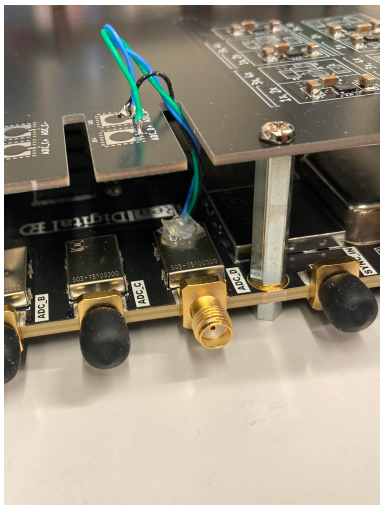


Figure 6.6: RFSoC ADC differential inputs connected to custom buffer PCB.

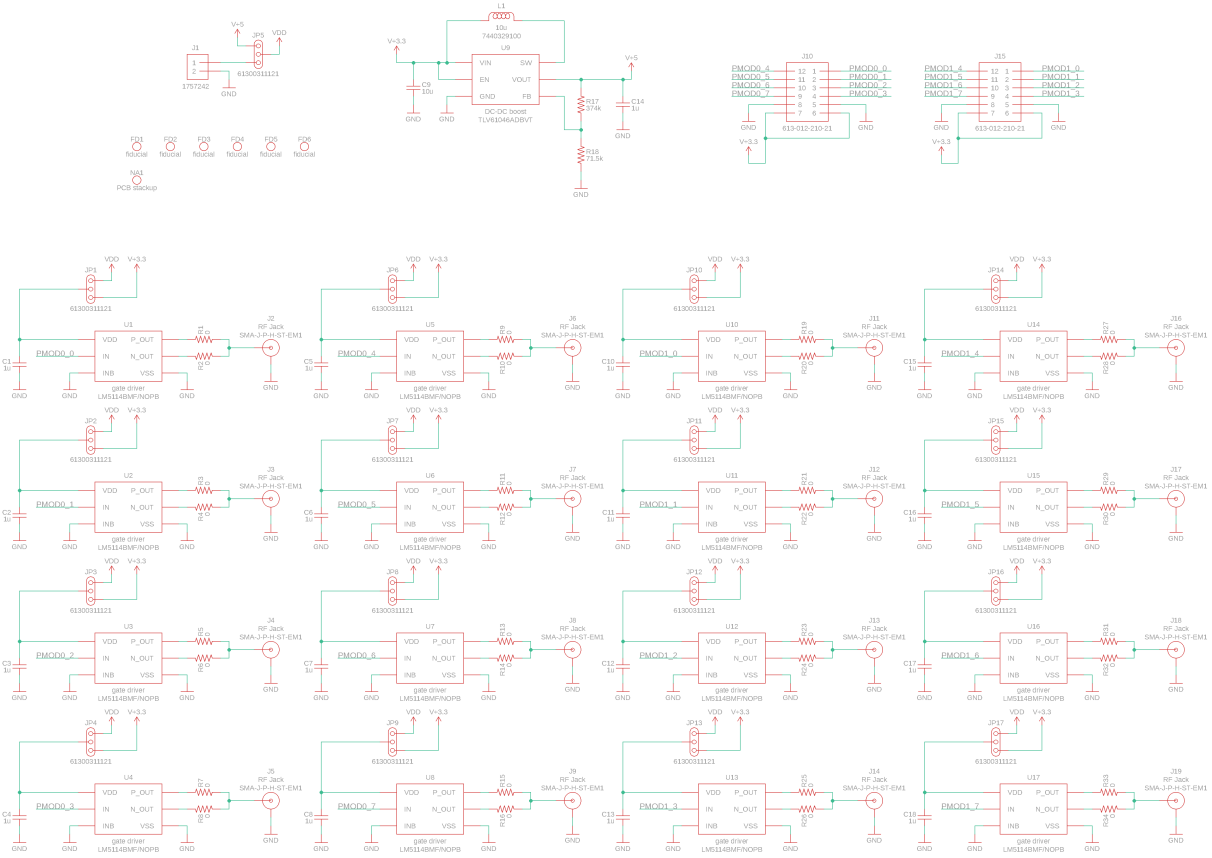


Figure 6.7: custom RFSoC digital output buffer PCB schematic.

need to be converted into a differential signal with the proper common-mode voltage. Figures 6.2 and 6.3 show the schematic and PCB, respectively, of the custom board designed for this purpose. In short, the board uses the LMH5401 to convert a single-ended, ground-referenced signal into a differential signal. Next, the RFSoC 4×2 needs to be modified. The differential outputs from the custom buffer PCB are wired directly into the ADC inputs of the RFSoC, as shown in figures 6.4 - 6.6 by removing C302 and C303 (for ADC_D), bypassing the balun.

6.2.4 Digital output buffer PCB

The RFSoC 4×2 has a PMOD connector with 3.3 V digital outputs. However, these outputs do not have sufficient strength to drive 50-ohm TTL loads, which are common in trigger inputs for lab instrumentation like laser drivers. Therefore, a custom board was designed



Figure 6.8: custom RFSoC digital output buffer PCB.

in order to buffer the PMOD digital output signals, as well as perform logic-level shifting. The board contains a LM5114BMF gate driver IC for each output pin, which is able to drive 50-ohm loads with < 5 ns rise time. The board can be powered by the 3.3 V rail provided by the 4×2, which is shifted to 5 V for TTL compliance, or by an external power supply.

6.2.5 QICK pulse compiler

Creating a pulse sequence using QICK can be challenging because the tproc is programmed using assembly code. The default QICK software package contains a python library that allows the user to generate assembly code for the tproc. However, this python library is designed to address the problems posed by superconducting qubit experiments, and is difficult to use for optically-addressable spin qubits. QICK pulse compiler was created to address this challenge, and provides the user with a platform to create high-level pulse sequence programs defined using python. Figures 6.9 and 6.10 show a snippet of python and the corresponding assembly code, respectively, which implement an optically-detected magnetic resonance pulse sequence.

```python
with QickScope(code=self):
    self.freq_reg = QickSweptReg(
        start=QickFreq(freq_start, gen_ch=dac_channels['sample_wg']),
        stop=QickFreq(freq_stop, gen_ch=dac_channels['sample_wg']),
        step=QickFreq(freq_step, gen_ch=dac_channels['sample_wg'])
    )

    mw_on = \
        init + \
        Delay(length=mw_pre_padding, name='mw pre padding') + \
        RFPulse(
            ch=dac_channels['sample_wg'],
            length=mw_len,
            offset=mw_offset,
            freq=self.freq_reg,
            amp=amp,
            name='mw'
        ) + \
        Delay(length=mw_post_padding, name='mw post padding') + \
        readout

    mw_off = \
        init + \
        Delay(length=mw_pre_padding, name='mw pre padding') + \
        Delay(length=mw_len, name='no mw') + \
        Delay(length=mw_post_padding, name='mw post padding') + \
        readout

    mw_on.inc_ref()
    experiment = mw_on + mw_off

    freq_sweep = QickSweep(
        code=experiment,
        reg=self.freq_reg,
        inc_ref=True
    )

    experiment_loop = QickLoop(
        code=TrigPulse(
            ch=trig_channels['tt_3'],
            length=200e-9,
            name='tt_sync'
        ) | freq_sweep,
        loops=loops,
        name='loop',
        inc_ref=False,
    )

```

Figure 6.9: QICK pulse compiler python code implementing an optically-detected magnetic resonance pulse sequence.

```
NOP
TIME inc_ref #49152
LOOP_2:
REG_WR out_usr_time imm #0
TRIG set p11
REG_WR out_usr_time imm #98
TRIG clr p11
REG_WR r0 imm #1523712000
REG_WR r1 imm #1523766613
REG_WR r2 imm #5461333
SWEEP_0:
TEST -op(r0 - r1)
JUMP SWEEP_END_1 -if(NS)
REG_WR out_usr_time imm #-522
TRIG set p0
REG_WR out_usr_time imm #-276
TRIG clr p0
REG_WR out_usr_time imm #292
REG_WR w_length imm #49
REG_WR w_gain imm #32700
REG_WR w_freq op -op(r0)
REG_WR w_phase imm #0
REG_WR w_conf imm #9
WPORT_WR p0 r_wave
REG_WR out_usr_time imm #114
TRIG set p4
REG_WR out_usr_time imm #703
TRIG clr p4
REG_WR out_usr_time imm #-153
TRIG set p5
REG_WR out_usr_time imm #442
TRIG clr p5
REG_WR out_usr_time imm #290
TRIG set p10
REG_WR out_usr_time imm #388
TRIG clr p10
REG_WR r4 imm #934
TIME inc_ref r4
REG_WR out_usr_time imm #-522
TRIG set p0
REG_WR out_usr_time imm #-276
TRIG clr p0
REG_WR out_usr_time imm #114
TRIG set p4
REG_WR out_usr_time imm #703
TRIG clr p4
REG_WR out_usr_time imm #-153
TRIG set p5
REG_WR out_usr_time imm #442
TRIG clr p5
REG_WR out_usr_time imm #290
TRIG set p10
REG_WR out_usr_time imm #388
TRIG clr p10
REG_WR r3 imm #934
TIME inc_ref r3
REG_WR r0 op -op(r2 + r0)
JUMP SWEEP_0
SWEEP_END_1:
JUMP LOOP_2
WAIT time @0
DMEM_WR [&0] imm #1
JUMP HERE
```

Figure 6.10: QICK assembly code corresponding to figure 6.9.

CHAPTER 7

CONTROL SOFTWARE (NSPYRE)

nspyre (Networked Scientific PYthon Research Environment) is an open-source python software package designed to give the user a set of useful tools for running scientific experiments. It provides features for controlling instruments, storing and plotting data, and generating a graphical-user interface (GUI). Instrument control and data processing are both performed over a network connection, which offers some advantages discussed below.

7.1 Instrument control

When designing custom instrumentation, such as the confocal microscope used in this work, it is common to have many disparate instruments that must all be controlled and properly configured. This can be a daunting task, as even a simple setup may consist of dozens of subcomponents. nspyre does not directly provide any instrument drivers or a common standard for writing instrument drivers (although, there is a separate repository that contains some instrument drivers). What it does provide is a set tools for interfacing with instrument drivers across a network connection. While it is usually best to directly interface with an instrument driver, this is occasionally not possible or desirable. nspyre provides the *InstrumentServer* and *InstrumentManager* for this purpose, which are basically wrappers around the rpyc remote procedure call package. They allow the user to easily host a set of instrument drivers on one system using the *InstrumentServer*, and then interface with those instrument drivers over a network connection with the *InstrumentManager* (which may be running on the same system as the *InstrumentServer*, or a different one). There are several common situations in which this might be helpful. Some instruments have dedicated control computers, which may not be where the user wants to run their experiment code. Furthermore, an instrument may be utilized by different researchers in different experiments.

In this case, it may be convenient to have a computer that controls the instrument, and then each user can remotely connect to this computer to control the instrument. Another situation in which it might be helpful is if an instrument driver must perform some sort of lengthy or inconvenient initialization sequence each time it's created. By hosting that instrument driver on an *InstrumentServer*, it can be initialized once and then controlled in many subsequent experiments with an *InstrumentManager* without the driver being deinitialized.

7.1.1 InstrumentServer

Creating an instrument server is quite simple. The user starts up the server, and then instantiates drivers with the *add()* method as demonstrated below.

```
from pathlib import Path

from nspyre import serve_instrument_server_cli
from nspyre import InstrumentServer

HERE = Path(__file__).parent

# create a new instrument server
with InstrumentServer() as inserv:
        # add signal generator driver
        # 'sg' will be an instance of the class 'SigGen' in the file ./drivers/sg.py
        inserv.add('sg', HERE / 'drivers' / 'sg.py', 'SigGen')
        # add data acquisition instrument driver
        # 'daq' will be an instance of the class 'DAQ' in the file ./drivers/daq.py
        inserv.add('daq', HERE / 'drivers' / 'daq.py', 'DAQ')

        # run a CLI (command-line interface) that allows the user to enter
        # commands to control the server
        serve_instrument_server_cli(inserv)
```

7.1.2 InstrumentManager

Connecting to an instrument server and controlling the associated instruments is equally simple, demonstrated below.

```
from nspyre import InstrumentManager

# connect to an instrument server
with InstrumentManager() as manager:
        manager.sg.set_amplitude(5)
        manager.sg.set_frequency(5)
```

7.2 Data processing

nspyre provides a set of tools that make the pipeline of data collected in an experiment more robust and convenient to process. One desirable property of this data pipeline is that the user can view and process data continuously in real time without affecting the experiment. Another desirable property is the ability to view the data in multiple ways, or remotely from a different system than the one running the experiment. Like the instrument control, nspyre accomplishes this using network connections. There are three components that are used for processing data: a "source", the data server, and a "sink". The data source provides data, the data server buffers and duplicates the data, and the sink receives the data, which the user can then process and plot. The source and sink connect to the data server over a network connection. The data server acts like a buffer, minimizing any affect of the data sink on the source.

7.2.1 DataSource

The data pipeline begins in the code running the experiment, demonstrated below.

```
from nspyre import DataSource

with DataSource('MyDataSet') as data_source:
        my_data = []
        while experiment_is_running():
                # collect some data
                my_data.append(some_instrument.get_new_data())
                # send the data to the data server
                data_source.push({
                        'some_data': my_data,
                })
```

Data is continuously collected from an experiment, and then pushed to the data server by the *DataSource*. Each data source is associated with a specific named *Data Set*, in this case *MyDataSet*. Only one *DataSource* can be pushing data to a *Data Set* at time.

7.2.2 DataSink

Any number of *DataSink* may be created and sink data from a single *Data Set*, since the data pipeline may be duplicated in the data server. Retrieving data from a data set is demonstrated below.

```
from nspyre import DataSink

with DataSink('MyDataSet') as data_sink:
        while user_wants_to_plot():
                data_sink.pop()
                update_my_plot(data_sink.some_data)
```

7.2.3 StreamingList

The reader may have noticed that in the *DataSource* example the entire set of collected data is sent to the data server on each call to *push()*. In the case that there is a large amount of data being collected, this redundancy may demand significant network and memory costs, and quickly become unmanageable. To solve this problem, there is a special "streaming" class demonstrated below.

```
from nspyre import DataSource
from nspyre import StreamingList

with DataSource('MyDataSet') as data_source:
        my_data = StreamingList([])
        while experiment_is_running():
                # collect some data
                my_data.append(some_instrument.get_new_data())
                # send the data to the data server
                data_source.push({
                        'some_data': my_data,
                })
```

All that has changed from the original code is that the *StreamingList* has been used as a drop-in replacement for a python list, which makes things quite simple for the user. Under the hood, the streaming list overrides the common list operations, such as *append()*, and detects what changes the user has made to it between each call to push(), allowing it to only send *changes* to the data server, rather than *all* of the data. At the moment, only the list data type is implemented, although others may be implemented in the future.

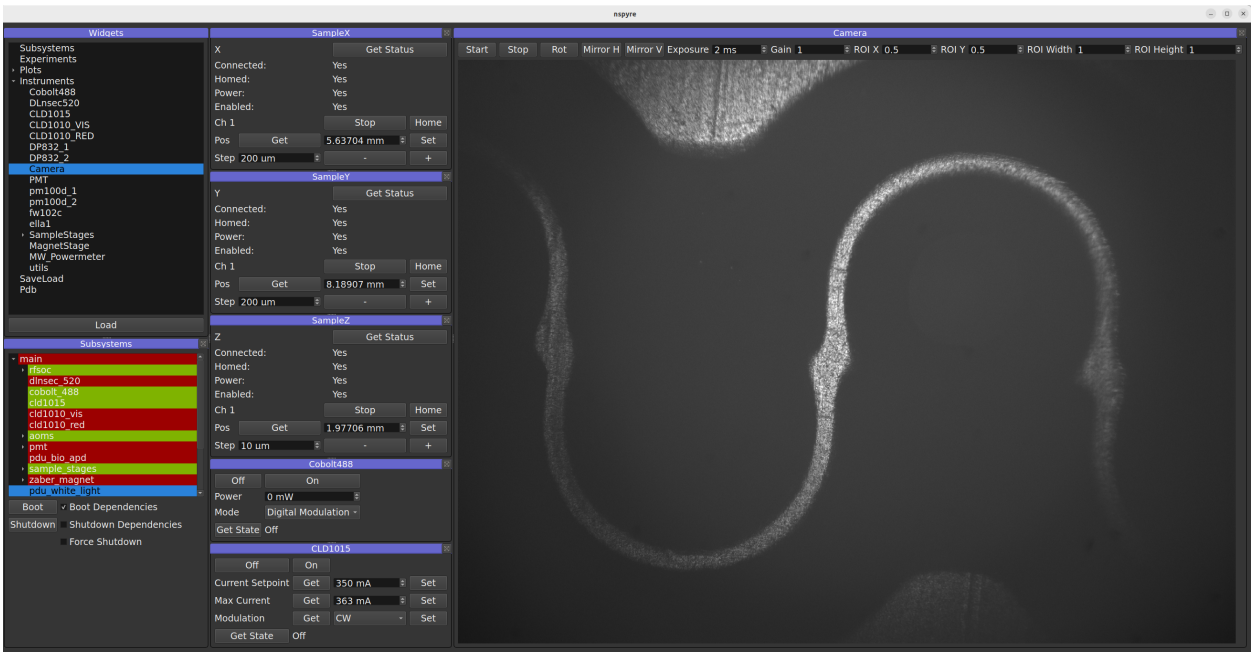


Figure 7.1: GUI made using nspyre for the experiments performed in this work.

7.3 Graphical user interface

Finally, nspyre provides a set of functionality for generating graphical user interfaces (GUIs) for controlling the experiment and visualizing data. The GUI components are built on PyQt and PyQtGraph, which provide the core GUI library, and plotting functionality, respectively. Figure 7.1 shows some of the GUI widgets developed for the experiments in this thesis. The subsystems widget allows the user to control the power state of all subsystems, and automatically handles power supply sequencing and dependencies. For example, booting or shutting down the "rfsoc" subsystem will automatically boot or shut down all of its associated components in the proper sequence, such as the microwave preamp and power amplifier, DC power supplies for the digital and analog buffer PCBs, as well as a secure shell tunnel for remotely connecting to the RFSoC onboard processor. There are also widgets for controlling other instruments such as the X, Y, and Z stages for adjusting the sample position, the laser drivers, and a widefield camera for aligning the confocal laser spot with the desired measurement area. Figure 7.2 shows an nspyre template project demonstrating nspyre's

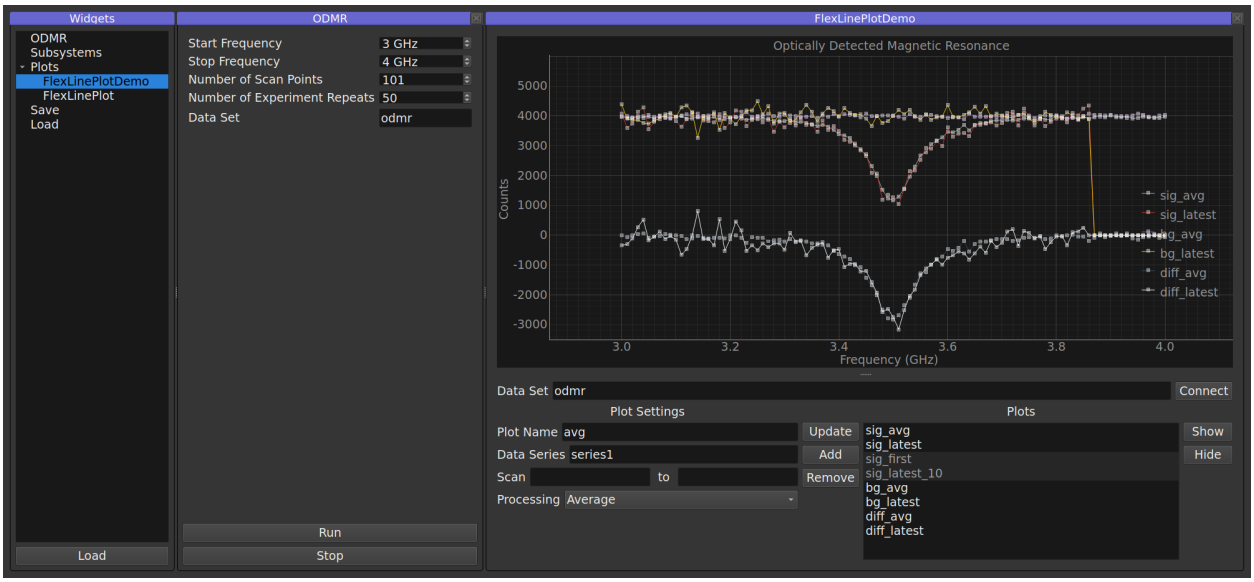


Figure 7.2: Example GUI made using nspyre demonstrating live plotting functionality.

built-in plotting functionality. The "ODMR" widget generates mock data, which is plotted by the "FlexLinePlotDemo" widget. The plot updates in real-time, and allows the user to simultaneously view different slices of the data, such as the first or last scan, or all scans averaged together.

CHAPTER 8

FLUORESCENT-PROTEIN SPIN QUBITS

This chapter and figures were adapted from the following [15]:

Jacob S. Feder*, Benjamin S. Soloway*, et al. *arXiv preprint* quant-ph 2411.16835.

(*Equal contribution)

Optically-addressable spin qubits form the foundation of a new generation of emerging nanoscale sensors [16–20]. The engineering of these sensors has mainly focused on solid-state systems such as the nitrogen-vacancy (NV) center in diamond. However, NVs are restricted in their ability to interface with biomolecules due to their bulky diamond host. Meanwhile, fluorescent proteins have become the gold standard in bioimaging, as they are genetically encodable and easily integrated with biomolecules [21–23]. While fluorescent proteins have been suggested to possess a metastable triplet state [2], they have not been investigated as qubit sensors. Here, we realize an optically-addressable spin qubit in the enhanced yellow fluorescent protein (EYFP) enabled by a novel spin-readout technique. A near-infrared laser pulse allows for triggered readout of the triplet state with up to 44% spin contrast. Using coherent microwave control of the EYFP spin at liquid-nitrogen temperatures, we measure a spin-lattice relaxation time of $(141 \pm 5)\,\mu s$, a $(16 \pm 2)\,\mu s$ coherence time under Carr-Purcell-Meiboom-Gill (CPMG) decoupling, and predict an oscillating (AC) magnetic field sensitivity with an upper bound of $183\,\mathrm{fTmol}^{1/2}\mathrm{Hz}^{-1/2}$. We express the qubit in mammalian cells, maintaining contrast and coherent control despite the complex intracellular environment. Finally, we demonstrate optically-detected magnetic resonance at room temperature in aqueous solution with contrast up to 3%, and measure a static (DC) field sensitivity with an upper bound of $93\,\mathrm{pTmol}^{1/2}\mathrm{Hz}^{-1/2}$. Our results establish fluorescent proteins as a powerful new qubit sensor platform and pave the way for applications in the life sciences that are out of reach for solid-state technologies.

Optically-addressable quantum sensors capable of measuring nanoscale magnetic fields [24–26], electric fields [27], and temperature [28–30] have had a lasting impact on the physical sciences [16, 31–34]. In contrast, their adoption in the life sciences has been limited, with most applications remaining at the proof-of-concept stage. A molecule-scale spin qubit sensor that can be readily interfaced with biological target systems could enable a new generation of ultra-sensitive measurement techniques for fundamental research and medical diagnostics [18, 19].

The leading spin qubit for biological sensing is the nitrogen-vacancy (NV) center in diamond because it has a spin that can be optically initialized and read out, remains coherent at room temperature, and can be hosted in diamond nanoparticles. Nanodiamonds suffer from problems common to nanoparticle labeling [35] since they are heterogeneous in size and morphology, have complex surface chemistry, and are ten times larger than an average protein [36, 37]. These issues have made cellular delivery and specific targeting an outstanding challenge. Optically-addressable molecular spin qubits, such as polycyclic aromatic hydrocarbons [38–41], metal-organic complexes [42–44], and radical systems [45, 46], offer potential advantages over NV centers. However, the systems examined thus far each have their own set of shortcomings, which include low spin contrast, poor photon-emission rates, lack of water solubility, the requirement of a solid-state host, or reactivity with ambient air, limiting their applicability for most biosensing applications.

Fluorescent proteins derived from the jellyfish *Aequorea victoria* are a ubiquitous tag for biological imaging [21–23]. They have a high absorption cross section and quantum yield, and a short fluorescence lifetime, resulting in bright emission. The ability to be genetically encoded makes them ideal for dense labeling of living cells and organisms, with specificity beyond what can be achieved with synthetic molecular fluorophores or nanoparticles [23]. Decades of research has generated a vast library of fusion proteins consisting of fluorescent proteins deterministically tagged to biological targets. Interestingly, the photoactive organic

fluorophore embedded in the fluorescent proteins' beta barrel possesses a metastable state that has been suggested to be a spin triplet [2]. If harnessed as a qubit, this intrinsic spin could unlock new quantum sensing modalities for fluorescent proteins.

8.1 Protein qubit and spin readout

Here, we use a custom confocal microscope (figure 8.1a) to optically address the metastable triplet spin state of the EYFP (figure 8.1b). The EYFP spin is initialized with a 488 nm optical pulse, cycling the fluorophore between its ground (S_0) and first-excited (S_1) singlet state, which then undergoes intersystem crossing (ISC) to a spin-polarized metastable triplet (T_1). Time-dependent density functional theory (TDDFT) calculations show that the T_1 spin density is fully delocalized on the chromophore (figure 8.1d). However, this metastable triplet presents challenges in its use as a spin qubit. Readout of the spin via the triplet decay is precluded by spin depolarization at most temperatures, which is fast compared to the millisecond-scale triplet lifetime [2, 47]. The extended triplet lifetime also limits the measurement sequence repetition rate, placing a bottleneck on the sensitivity.

We overcome the aforementioned challenges associated with the metastable triplet by utilizing a photophysical technique to shorten its lifetime [12, 48] and enable on-demand spin readout (figure 8.1c). A 912 nm optical pulse drives the fluorophore from its triplet T_1 state to a higher-lying triplet. TDDFT calculations (Methods) suggest the identity of this triplet to be the T_2 state. Spin-dependent reverse intersystem crossing (RISC) to the singlet manifold is accelerated in this state. Following RISC, a background-free delayed fluorescence photon is emitted from S_1. Readout using this optically-activated delayed fluorescence (OADF) [34] scheme is approximately five orders of magnitude faster than via the metastable triplet decay.

We find that the OADF spectrum closely resembles the standard fluorescence spectrum at 80 K (figure 8.4a), which indicates that the delayed fluorescence photons are indeed emitted

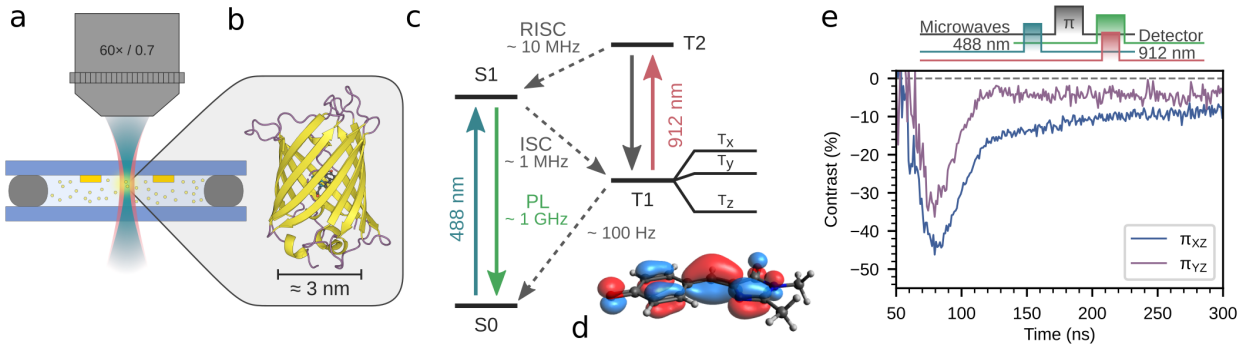


Figure 8.1: **(a)** Schematic representation of purified optically-addressable EYFP spin qubits (yellow) encapsulated in a liquid cell, which is composed of sapphire coverslips (blue) sealed with an o-ring (dark gray). The sample is imaged in a custom-built confocal microscope (figure 8.2). A microscope objective (gray) focuses gated laser beams of 488 nm (light blue) and 912 nm (red) wavelengths to an approximately 5 µm diameter focal spot. A lithographically patterned microwave structure (gold) is used for coherent driving of the EYFP spins. **(b)** Ribbon diagram of EYFP (Protein Data Bank: 2YFP [3]). **(c)** Energy-level diagram of EYFP with OADF readout scheme. **(d)** The natural transition orbital structure for the T_1 state, calculated by ab initio calculations. **(e)** Contrast of OADF-based spin readout as a function of time after the 912 nm laser pulse for the $T_x - T_z$ (blue) and $T_y - T_z$ (purple) transition. The measurement sequence above the figure illustrates the timing of the microwave and optical pulses. The "Detector" channel represents the timing of the acousto-optic modulator used to gate the detector. Panel (e) is measured at 80 K.

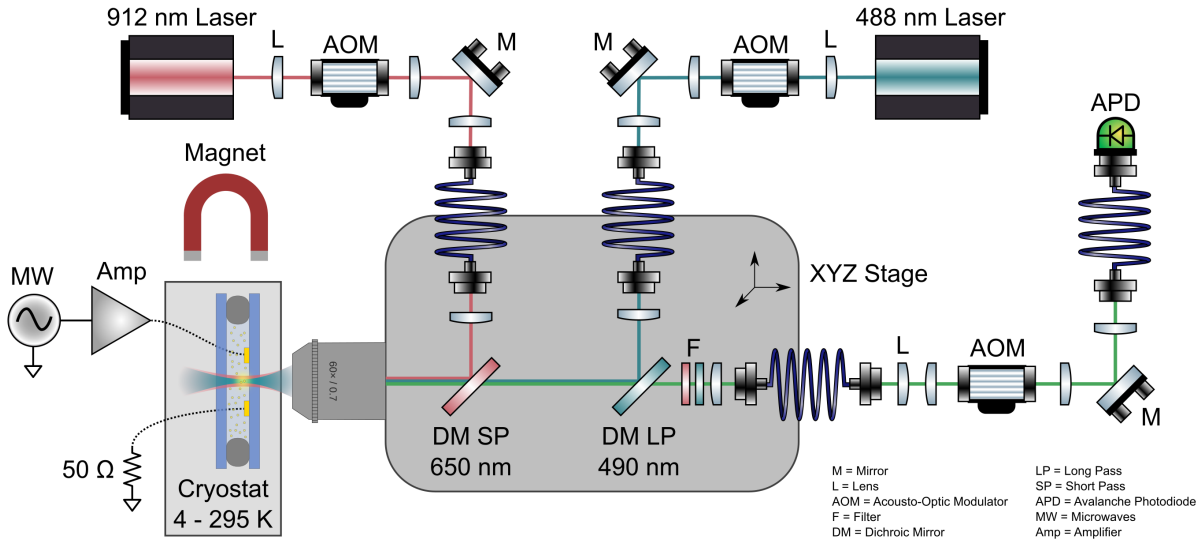


Figure 8.2: 488 nm and 912 nm diode lasers are gated using acousto-optic modulators (AOMs) and coupled into single-mode fibers. The fibers deliver laser light to a movable optical assembly for scanning over the sample. Dichroic mirrors overlap the excitation beams such that they are focused to the same spot by the microscope objective (60×, 0.7 NA). The optical powers at the back of the objective for the 488 nm and 912 nm lasers are about 0.4 mW and 65 mW, respectively. Light collected from the sample passes through the dichroic mirrors and filters for removing the laser light, and is focused onto a single-mode fiber. The fiber acts as a pinhole, filtering out-of-focus light such that the signal is primarily from proteins illuminated with the highest laser intensities. After being gated by an AOM, the collected light is detected by a single-photon counting module or, in figure 8.4a, a spectrometer. The sample is mounted in a custom imaging cell that holds 5 µL. It encapsulates the sample between two 500 µm thick sapphire windows, sealed by an o-ring. The sapphire substrate nearer to the cryostat window is photolithographically patterned with microwave loop structures using a lift-off process. The cryostat is evacuated to < 1 Torr and subsequently cooled following a temperature profile similar to 8.3b. An external DC magnetic field is applied using a permanent magnet attached to a motorized translation stage outside of the cryostat. The microwave output of the RFSoC is fed into a series of amplifiers before being delivered to the loop structures. The microwave power before entering the cryostat was approximately 1 W.

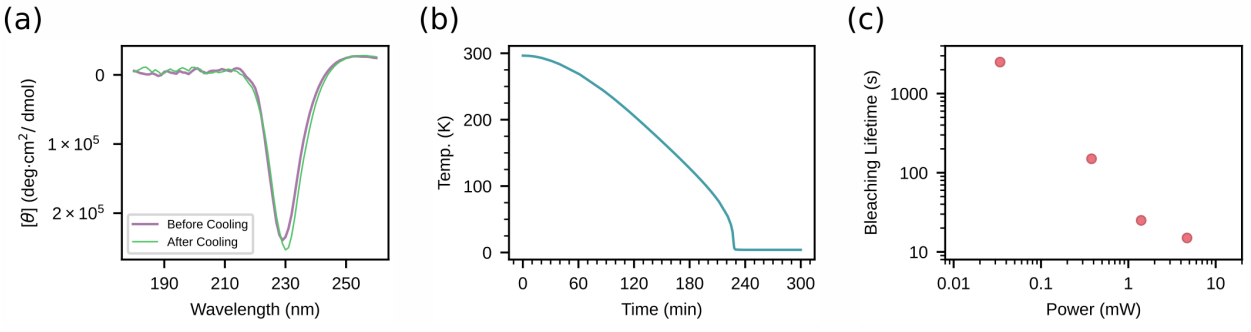


Figure 8.3: **(a)** Circular dichroism measurement taken on protein just after expression (before cooling), and after a full measurement sequence consisting of loading into the sample holder, cooling to cryogenic temperatures, and warming back up to room temperature (after cooling). **(b)** Cooling profile of the cryostat platform. **(c)** Bleaching lifetime of the protein versus laser power measured at the back of the objective. Panel (a) was measured at room temperature and (c) was measured at 4 K.

from the S_1 to S_0 transition. Furthermore, the wavelength of the intensity maxima at 80 K and room temperature are in good agreement, suggesting that the frozen protein maintains its structure in the vicinity of the fluorophore after being slowly cooled to cryogenic temperatures (figure 8.3a, b).

The addition of a microwave drive demonstrates the optical addressability of the spin state. After initialization, a microwave π-pulse induces population transfer between the spin sublevels in the T_1 state. Detection of the OADF photons triggered by the 912 nm laser pulse yields a maximum spin contrast of 44% for the $T_x - T_z$ transition and 32% for the $T_y - T_z$ transition at 80 K (figure 8.1e, 8.4b,c).

8.2 Optically-detected magnetic resonance

We investigate the nature of the metastable triplet spin state through optically-detected magnetic resonance (ODMR) spectroscopy. Figure 8.5a shows the ODMR contrast as a function of microwave frequency and external magnetic field. At zero field, we observe two characteristic resonances corresponding to the $T_y - T_z$ and $T_x - T_z$ transitions. Generally, for a spin-1 system we expect a Hamiltonian of the form

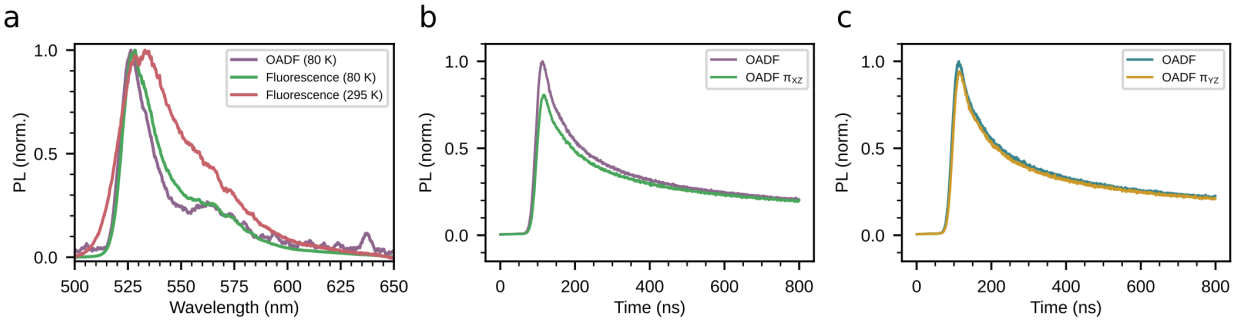


Figure 8.4: **(a)** The EYFP initialized with a 488 nm laser pulse, then the spectra of the collected light recorded during a subsequent 912 nm laser pulse (purple), as well as the fluorescence collected during continuous illumination with the 488 nm laser at 80 K (green) and 295 K (red). **(b)** After initialization, the time trace of the collected light near the rise of the 912 nm laser pulse without (purple), and with (green) a microwave π-pulse on the $T_x - T_z$ transition. **(c)** The same as (b), but on the $T_y - T_z$ transition. Panels (b), (c) are measured at 80 K.

$$H = \hbar D(S_z^2 - \frac{2}{3}) + \hbar E(S_x^2 - S_y^2) - \hbar\gamma_{el}\vec{S}\cdot\vec{B} \tag{8.1}$$

where $\hbar$ denotes the reduced Planck constant, D and E the zero-field splitting parameters (ZFS), $\gamma_{el} = (2\pi) \times 28\,\mathrm{GHz\,T^{-1}}$ the gyromagnetic ratio of an electron, $\vec{S}$ the vector of Pauli spin matrices for a spin-1 system, and $\vec{B}$ the magnetic field. Since the experiments are performed on a randomly oriented ensemble of EYFP molecules, we expect the ODMR signal to be an average over all molecular orientations, resulting in a powder spectrum [49]. Fitting at low magnetic fields (the region where the uncertainty in the field calibration is small, Methods), we extract the ZFS parameters $D = (2\pi) \times (2.356 \pm 0.004)\,\mathrm{GHz}$ and $E = (2\pi) \times (0.458 \pm 0.003)\,\mathrm{GHz}$. *Ab initio* calculations with the B3LYP-optimized geometry and B97X-D3 functional predict similar values, $D_{DFT} = (2\pi) \times 2.42\,\mathrm{GHz}$ and $E_{DFT} = (2\pi) \times 0.57\,\mathrm{GHz}$. Using the fitted D and E parameters, we calculate the expected spectra of the powder-averaged transition frequencies as a function of magnetic field (figure 8.5b). The overall magnetic-field dependent broadening and asymmetric resonance profile is well

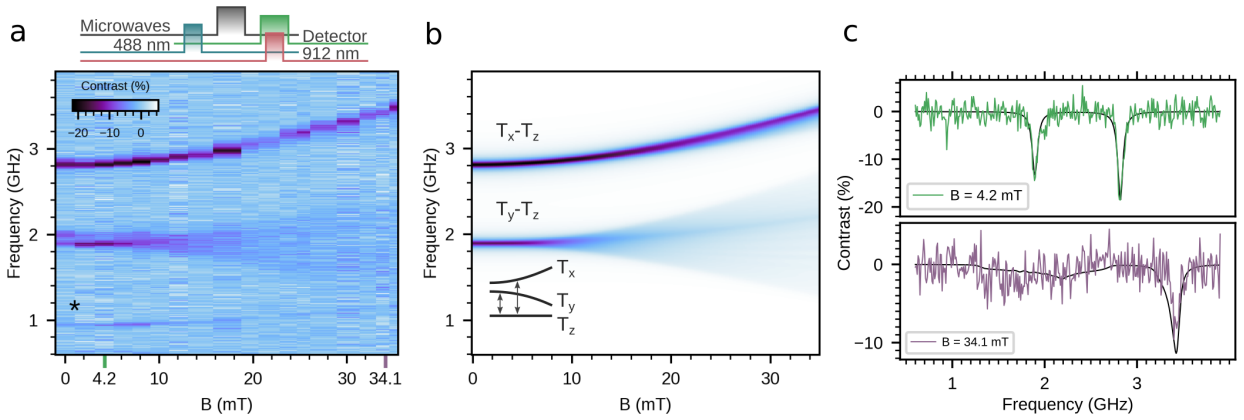


Figure 8.5: **(a)** Experimental ODMR signal as a function of externally applied magnetic field. The faint resonance (*) at approximately $= (2\pi) \times 0.9\,\text{GHz}$ is associated with microwave harmonics that drive the $T_x - T_z$ and $T_y - T_z$ transitions. **(b)** Simulated ODMR response based on the model from eq. 1. The fit parameters (D, E, linewidth of resonance, and $T_x - T_z$ and $T_y - T_z$ amplitudes) are extracted from an ODMR measurement at low magnetic fields (Methods). The ODMR amplitude for the $T_x - T_y$ transition is set to 0. For the resonance frequencies of the diagonalized Hamiltonian, see figure 8.6. **(c)** Experimental (green, purple) and simulated (black) ODMR spectrum at 4.2 mT and 34.1 mT. Panels (a), (c) are measured at 80 K.

captured by our model. It also extrapolates well to higher fields exemplified at 34.1 mT (8.5c bottom).

8.3 Qubit coherence

Driving the EYFP molecules with a fixed frequency that is resonant with the $T_x - T_z$ transition results in coherent Rabi oscillations between the spin sublevels (figure 8.7a). The oscillations are highly damped, with a decay rate that increases with Rabi frequency as a result of random molecular orientations and microwave drive detuning (figure 8.8).

We measure the spin coherence time (T_2) using a Hahn-echo sequence to refocus dephasing caused by quasi-static magnetic fields (figure 8.7b). With no applied field, the T_2 is $(1.5 \pm 0.2)\,\mu\text{s}$. We find that with increasing field, T_2 decreases to $(140 \pm 30)\,\text{ns}$ at 7 mT. The scaling of T_2 is a consequence of the $T_x - T_z$ resonance resembling a clock-like transition

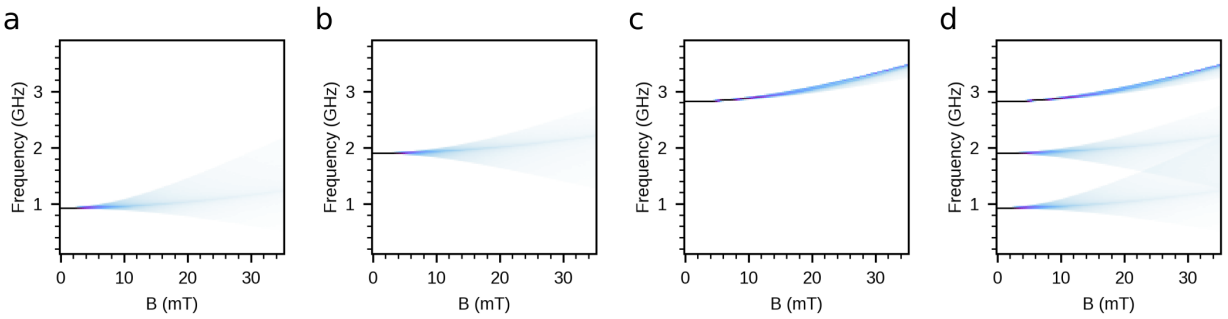


Figure 8.6: **(a)** Histogram of randomly oriented molecules' resonance frequencies for the $T_x - T_y$ as a function of applied magnetic field using the Hamiltonian in eq.-1. **(b)** Same as (a) but for the $T_y - T_z$ transition. Same as (a) but for the $T_x - T_z$ transition. **(d)** The sum of (a), (b), and (c). Some molecules' $T_y - T_z$ and $T_x - T_y$ transitions overlap at higher applied magnetic fields.

[50, 51], resulting in a dephasing rate $1/T_2 = \gamma_{eff} \propto \frac{\gamma B_z}{\sqrt{(E/\gamma_{el})^2 + B_z^2}}$. This rate is in good agreement with our observations (8.7b inset), suggesting that, in the vicinity of the clock transition, qubit dephasing remains primarily limited by magnetic rather than electric field noise.

Applying a CPMG sequence improves T_2 by shifting the dynamical decoupling filter function to higher frequencies [52]. With 240 π-pulses, we observe a T_2^{DD} of (16±2) µs at zero field (figure 8.7c), which represents a 15-fold enhancement compared to the T_2 determined using Hahn Echo. Repeating the CPMG measurement for different numbers of π-pulses (N) yields a scaling $T_2 \propto N^{0.4\pm0.03}$ (figure 8.7c inset), which provides insights into the magnetic noise properties and can be connected to a power spectral density $S(\omega) \propto \omega^{-2/3}$ [53].

We characterize the spin-lattice relaxation time and its dependence on temperature by measuring the spin contrast between the qubit initialized in T_z and T_x as a function of wait time. At 80 K, the spin polarization follows an exponential decay with a lifetime of (141±5) µs (8.7d). For an integer spin system, the depolarization rate is given by $\frac{1}{T_1} = AT + BT^7$, where A and B are the amplitudes of direct and Raman processes, respectively [49] (8.7d inset). This model provides a good fit to our data when the amplitudes are treated as free parameters, but unambiguous identification of the exact relaxation mechanisms will require

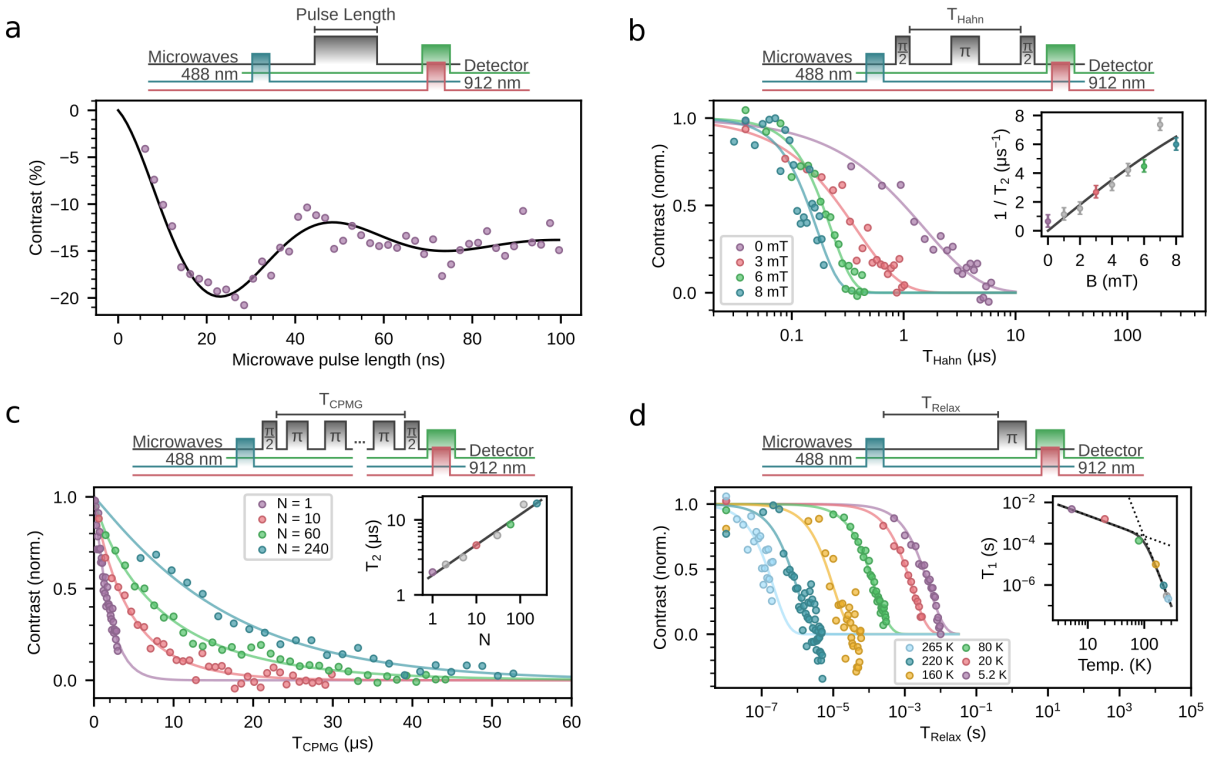


Figure 8.7: **(a)** Rabi oscillations of EYFP $T_x - T_z$ transition driven at a frequency of 2.815 GHz. The fit corresponds to an exponentially damped cosine (black). **(b)** Spin coherence as a function of total evolution time (T_{Hahn}) under Hahn-echo decoupling for different magnetic fields, with stretched-exponential fits. Inset shows the scaling of the Hahn-echo dephasing rate ($1/T_2$) as a function of external magnetic field and the corresponding theoretical model (black). **(c)** Same as in (b), but under a CPMG decoupling sequence for different numbers of π-pulses (N) and no external field. The inset shows T_2 scaling as a function of N and its corresponding fit (black). **(d)** Contrast as a function of evolution time (T_{Relax}) for different sample temperatures fit to exponential decays. Inset shows the spin-lattice relaxation time (T_1) as a function of temperature fitted with eq.-2, with fitted amplitudes $A = (43 \pm 8)\,\text{K}^{-1}\text{s}^{-1}$ and $B = (47 \pm 7) \times 10^{-12}\,\text{K}^{-7}\text{s}^{-1}$. In all plots, gray data points indicate additional measurements shown in the inset but not the main plot for clarity. The fit errors in the insets of panels (c) and (d) are smaller than the data points and omitted. Panels (a)-(c) are measured at 80 K.

a more thorough investigation.

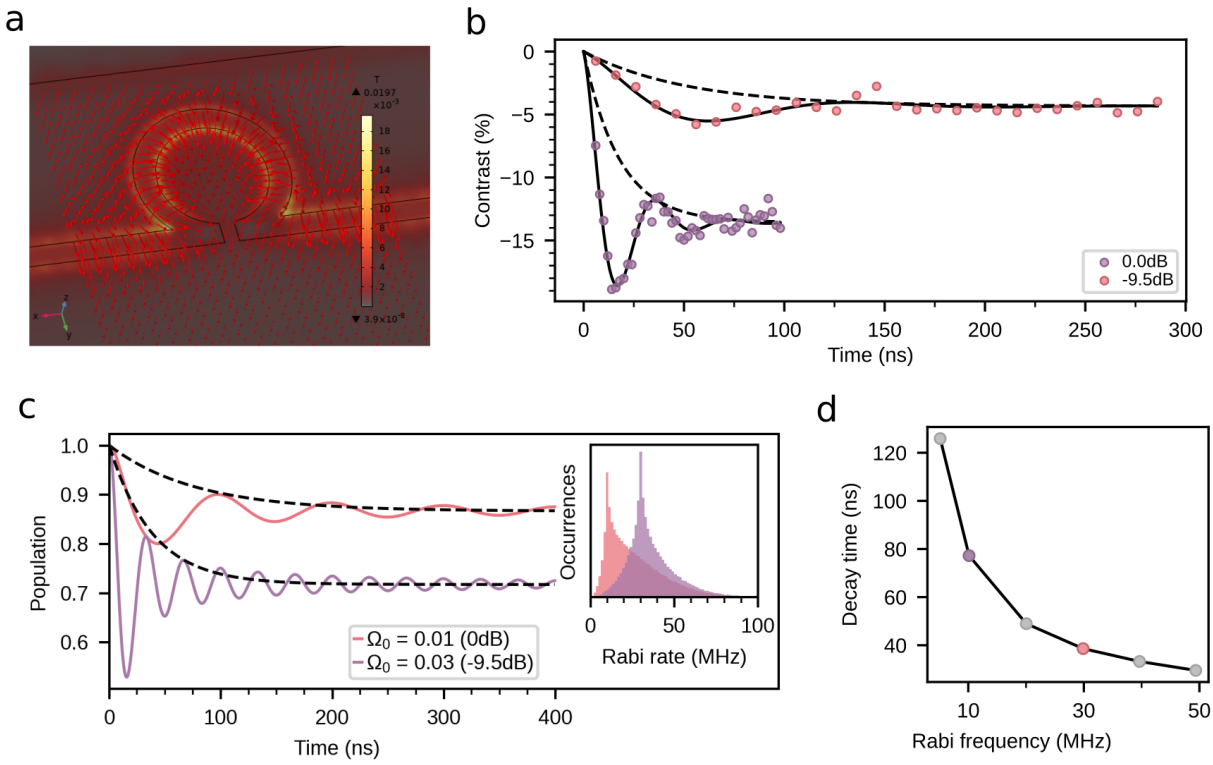


Figure 8.8: **(a)** Simulation of the magnetic flux density and field vectors generated from an omega waveguide. The field inhomogeneity across our optical spot at the center is negligible ($< 2\%$). **(b)** Experimentally observed Rabi oscillations fitted with a solid black line. The decay of the higher (lower) power Rabi oscillation is 18 ns (51 ns) and illustrated by a dashed black line. **(c)** Simulated average population of an ensemble of randomly oriented molecules assuming a linewidth $(2\pi) \times 33$ MHz. The decay of the higher (lower) power Rabi oscillation is 38 ns (77 ns) and illustrated by a dashed black line. The corresponding distributions of Rabi rates are shown in the inset. **(d)** Damped cosine fit parameters of the simulated Rabi oscillations. Note that the powers reported in the legends of (b) and (c) are not relative to each other. Panel (b) is measured at 80 K.

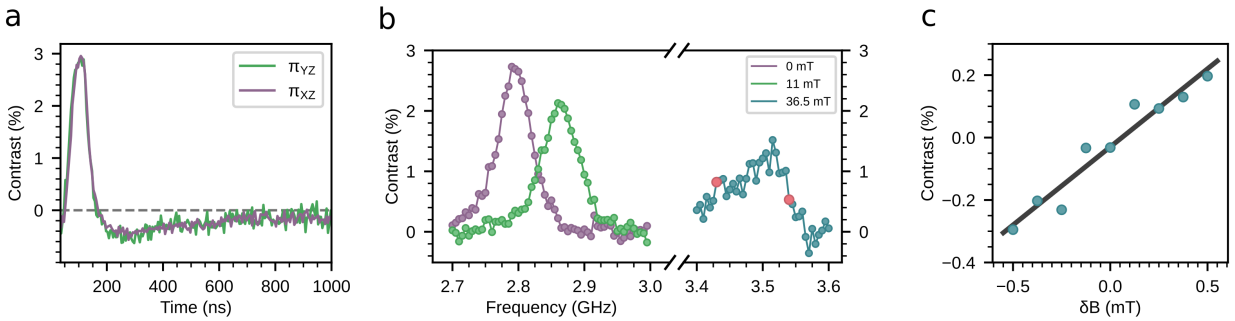


Figure 8.9: **(a)** Contrast of OADF-based spin readout as a function of time after the 912 nm laser pulse for the $T_y - T_z$ (green) and $T_x - T_z$ (purple) transition. **(b)** ODMR in aqueous solution at various magnetic fields. Red points indicate the locations of the field sensing experiment in (c). **(c)** DC magnetic field sensing operating at a bias field of 36.5 mT by measuring the difference in the ODMR signal at the two frequencies indicated in (b). Each data point has been averaged for 15 min. Panels (a)-(c) are measured at room temperature.

8.4 Operation at room temperature

Despite the fast spin relaxation extrapolated from our fit, we observe ODMR of EYFP in aqueous solution at room temperature with a contrast of nearly 3% (figure 8.9a, 8.9b). Interestingly, the sign of the spin contrast is reversed compared to measurements performed at 80 K, which suggests that spin-dependence of the ISC and/or RISC rates are temperature dependent. We confirm the magnetic origin of the resonance by repeating the experiment in the presence of an external field (8.9b). We demonstrate the potential of our qubit as a room-temperature DC magnetic field sensor following an approach adapted from the atomic clock community [54]. Detecting subtle shifts in the ODMR spectrum by measuring at two frequency points, one above and one below the $T_x - T_z$ resonance (figure 8.9b, right), results in a contrast difference that is a linear function of a small external magnetic field (δB) (figure 8.9c). From this measurement, we can estimate a DC magnetic field sensitivity of 98 pTmol$^{1/2}$Hz$^{-1/2}$ (Methods). The presence of a clock transition at zero field requires us to operate at a bias magnetic field.

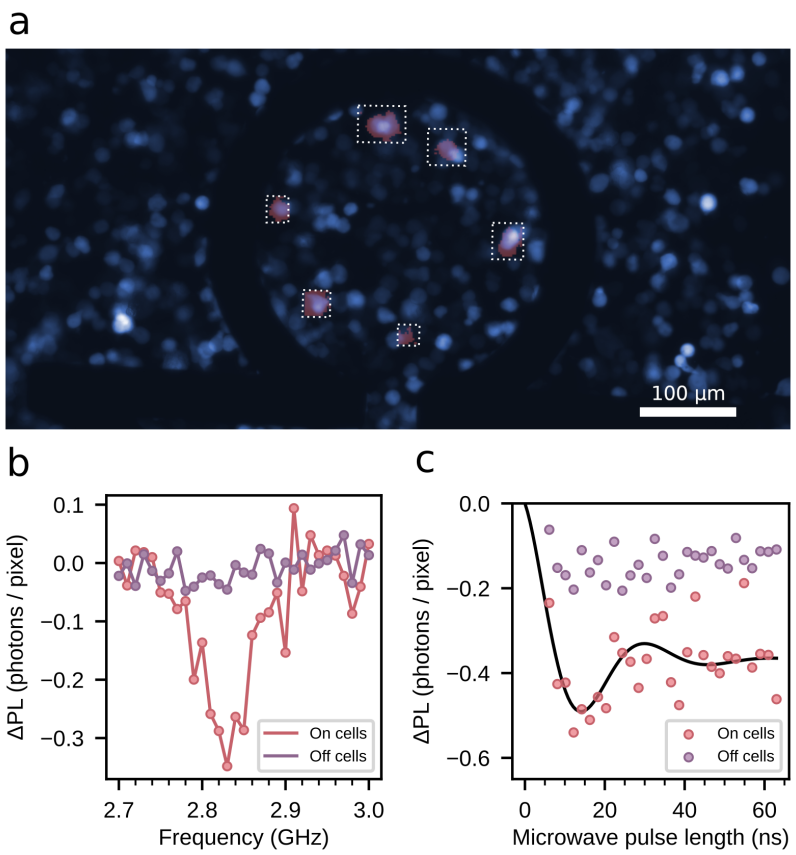


Figure 8.10: **(a)** A widefield fluorescence image of HEK 293T cells expressing cytosolic EYFP (blue). A loop structure for applying the microwave drive is visible. ODMR scans are taken in the white outlined regions, and thresholded for the brightest pixels (red). **(b)** ODMR signal averaged over the bright pixels (red, on cells) and dark pixels (purple, off cells). Instead of contrast, the PL difference normalized to the number of pixels is shown in order to illustrate the size of the signal contributed by the background. **(c)** Rabi signal taken with the same process as in (a), (b). Panel (a) widefield image is measured at room temperature. Red pixel overlay in (a), and panels (b), (c) are measured at 175 K.

8.5 Qubit sensor expressed in mammalian cells

We highlight the potential of *in vitro* applications of our genetically-encodable qubit by performing spin measurements on EYFP expressed in human embryonic kidney (HEK) 293T cells. Fluorescence imaging of the cells adhered to the sapphire substrate confirms that the protein remains localized within the cells (figure 8.10a). After cooling to 175 K, confocal fluorescence scans of the cells correlate well with the room-temperature widefield images (figure 8.11). Measuring over six bright regions containing cells, we record an ODMR signal (figure 8.10b, red). The OADF associated with these scans correlates well with the cells observed in widefield and confocal fluorescence images. Measuring only the pixels outside of cells results in a dim background signal, indicating that the spin resonance signature

originates from the bright cells rather than any extracellular EYFP. Repeating the same process, we drive Rabi oscillations in the cells (figure 8.10c). The ODMR and Rabi signals are consistent with those of the purified protein, confirming that the spin and optical interface are robust to operation within a cell.

8.6 Discussion and outlook

Our results establish fluorescent proteins as a genetically-encodable spin qubit platform with readout contrast, coherence, and spin-lattice relaxation times comparable to solid-state color centers. We estimate that EYFP has an upper-bounded AC sensitivity of $183\,\mathrm{fTmol}^{1/2}\mathrm{Hz}^{-1/2}$ at liquid-nitrogen temperatures (Methods) and an upper-bounded DC sensitivity of $93\,\mathrm{pTmol}^{1/2}\mathrm{Hz}^{-1/2}$ at room temperature. For reference, a proton spin located 5 nm away from the qubit – a practical distance for an EYFP fusion protein [55] – would generate a magnetic field of approximately 20 nT at the qubit's location. For a proton polarization p, these parameters translate into a proton number sensitivity of $\frac{1}{p}80\,\mathrm{pmol\,Hz}^{-1}$. While this sensitivity falls short of state-of-the-art NV diamond sensors [56], the ability to utilize the large existing library of genetically-encoded fusion proteins for in vitro and in vivo experiments provides significant advantages over diamond sensors.

Enhancements in sensitivity can be achieved by improving coherence or spin readout. At liquid-nitrogen temperatures, coherence is limited by magnetic-field noise, which can be drastically reduced by substituting nearby proton spins with deuterium, resulting in expected coherence times approaching 100 µs [57, 58]. Spin readout can be enhanced through two complementary strategies. First, initialization of the qubit requires an efficient population transfer from the singlet ground to the metastable triplet state. This can be improved by optimizing the excitation conditions and reducing unwanted RISC caused by the initialization laser [47, 59]. Second, OADF readout yields at most one photon per molecule. Combining OADF readout with fluorescence cycling in the singlet or triplet manifold could increase the

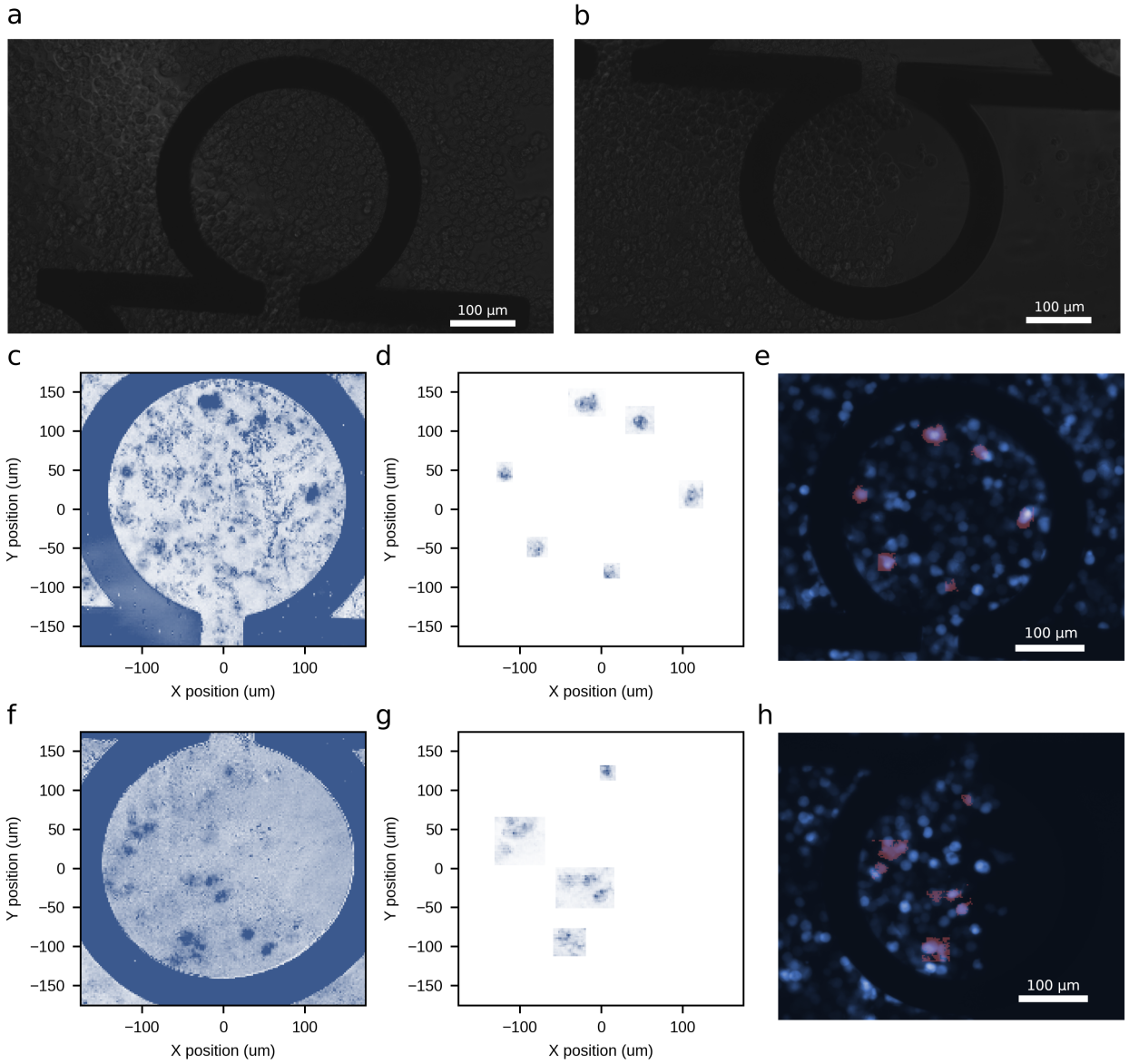


Figure 8.11: **(a)** Brightfield image corresponding to figure 8.10a. **(b)** Brightfield image of loop structure scanned in figure 8.10c to measure Rabi oscillations. **(c)** Confocal fluorescence image of (a). **(d)** OADF signal acquired during ODMR scan of selected areas in (c). **(e)** Zoom of figure 8.10a. **(f)** Same as (c) but on the loop structure in (b). **(g)** Same as (d) but corresponding to (f). **(h)** Same as (e) but with the thresholded pixels in (g). Panels (a), (b), (e), (h) were taken at room temperature. Panels (c), (d), (f), (g), and the red highlighted pixels in (e), (h) were taken at 175 K.

photon counts by 300-fold ($1/\phi_T$), where ϕ_T denotes the triplet yield [12, 47]). Optimizing the imaging optics could further improve per-molecule collection efficiency by a factor of 810.

Collectively, these improvements would yield at least a 500-fold improvement in AC and DC sensitivity. Finally, in addition to the above approaches for increasing the readout signal, combining our system with existing single-molecule microscopy techniques could enable the detection of individual EYFP qubit sensors [60], paving the way to single-molecule spin experiments.

Our on-demand readout method unlocks a large class of metastable triplet systems as qubits. In addition to EYFP, optically-activated RISC has been observed in many fluorescent proteins and dye molecules [12, 48]. In fact, systems comprising a singlet ground and excited state coupled to a metastable triplet are ubiquitous among fluorescent molecules, many of which may possess the requisite photophysical parameters for their metastable triplet to be addressed using our spin-readout technique. The exploration of these molecules may be accelerated by the computational methods demonstrated here for predicting the optical transitions and ZFS parameters.

The quantum information science and bioengineering fields have developed a diverse array of approaches to engineering complex systems. For example, the creation of highly regular structures through molecular self-assembly [61] could allow for the engineering of one-, two-, and three-dimensional paramagnetic molecular arrays [62]. The many-body dynamics of these spin systems could be optically read out with a protein qubit. Furthermore, traditional quantum engineering approaches to improving optical properties and spin coherence rely on gaining an understanding of qubit physics from first principles. Genetically-encodable probes like EYFP can be engineered using directed evolution, a black-box optimization approach that uses high-throughput screening of protein variants. Directed evolution of fluorescent proteins has resulted in a vast array of different spectral properties and functions, which highlight their tunability and rich photophysics [7]. Directed evolution on our EYFP qubit could be used to optimize its optical and spin properties, and even reveal unexpected insights into qubit physics. Protein-based qubits are positioned to take advantage of techniques from

both quantum information sciences and bioengineering, and produce transformative advances in both fields.

8.7 Protein expression and purification

The EYFP measured in aqueous solution contained the mutations S2insL / S65G / V68L / S72A / T203Y / H231L of avGFP, with an additional 6× His tag on the N-terminus (the full amino acid sequence is given at the end of this section). The protein was expressed using a pET vector constructed using HiFi assembly from Addgene plasmids #78466 and #29653. The resulting vector was sequenced to confirm the inclusion of the EYFP gene. The plasmid was transformed into BL21 (DE3) E. coli for protein expression. Single colonies of the cells were picked from a kanamycin plate and incubated in 5 mL of LB medium at 37 °C, 250 rpm overnight. Cultures were transferred into a 2 L flask with 500 mL of LB medium and continued incubating at 37 °C. Once the OD600 reached ~ 0.6, protein expression was induced with IPTG and the temperature was lowered to 30 °C. Cells were pelleted, and lysed using 4 mL of B-PER (Thermo Scientific) per gram of cells. The supernatant pre- and post-lysis appeared yellow and was loaded onto a Ni-NTA spin column (Thermo Scientific) and washed 3x using 10 mL of solution containing 50 mM sodium phosphate buffer, 500 mM NaCl, and 25 mM imidazole. Elution buffer (50 mM sodium phosphate buffer, 500 mM NaCl, and 250 mM imidazole) was used to elute the purified protein from the column. Buffer exchange using a 3 kDa molecular weight cut-off ultracentrifugal unit suspended the protein in the sample buffer (50 mM tris, 150 mM NaCl, 2 mM EDTA). The protein solution was concentrated, estimated to be 6 mM by measuring the optical density of the samples at 515 nm, and stored at −80 °C. When measured at cryogenic temperatures, the protein solution was mixed with 20% v/v DMSO.

The following is the amino acid sequence of the EYFP we measured from E. coli:

MGSSHHHHHHENLYFQSNIMLSKGEELFTGVVPILVELDGDVNGHKFSVSGEGE

GDATYGKLTLKFICTTGKLPVPWPTLVTTFGYGLQCFARYPDHMKQHDFFKSAMP
EGYVQERTIFFKDDGNYKTRAEVKFEGDTLVNRIELKGIDFKEDGNILGHKLEYNY
NSHNVYIMADKQKNGIKVNFKIRHNIEDGSVQLADHYQQNTPIGDGPVLLPDNHYLS
YQSALSKDPNEKRDHMVLLEFVTAAGITLGMDELYKSTGSG*

8.8 EYFP expression in mammalian cells

Plasmid pNWA171 encodes a second generation Chimeric Antigen Receptor(CAR) targeting CD19. The vector and a gene fragment encoding EYFP (Twist Bioscience) were both digested with MulI and SbfI restriction enzymes and then ligated with T4 ligase. The resulting plasmid was sequenced to confirm the inclusion of the EYFP gene and the deletion of the CAR19 gene. The plasmid was maxi-prepped, transfected with Lenti-X 293T cell line (Takara Bio) with PEI max (Polysciences), and then cultured for 48h for EYFP production. On the day of the experiment, a coverslip with photolithographically patterned waveguides was sterilized using 70% isopropanol, washed extensively with PBS, and then incubated with 0.01% poly-L-Lysine (MilliporeSigma) solution for 5 minutes. The residual polylysine solution was washed extensively with PBS. Cells were dissociated from the culture flask with trypLE (Gibco, Thermo Fisher Scientific) and then resuspended in DMEM supplemented with 10% HIFBS with a cell density of 1×10^7 cells/mL. Finally the cell suspension was incubated on the coverslip under 37 °C, 5% CO_2 for 3 hours. The coverslip was gently washed allowing only the adherent cells to remain for the experiments in figure 8.10.

The following is the amino acid sequence of the EYFP expressed in mammalian cells:

MLSKGEELFTGVVPILVELDGDVNGHKFSVSGEGEGDATYGKLTLKFICTTGKL
PVPWPTLVTTFGYGLQCFARYPDHMKQHDFFKSAMPEGYVQERTIFFKDDGNYK
TRAEVKFEGDTLVNRIELKGIDFKEDGNILGHKLEYNYNSHNVYIMADKQKNGIKV
NFKIRHNIEDGSVQLADHYQQNTPIGDGPVLLPDNHYLSYQSALSKDPNEKRDHMV
LLEFVTAAGITLGMDELYK*

8.9 Experimental methods

Experiments are performed in a closed-cycle liquid helium cryostat with temperature control from 4 K to room temperature using a custom confocal microscope (figure 8.2). Prolonged exposure to laser excitation results in photobleaching of the EYFP (figure 8.3c). To counteract photobleaching, the microscope is scanned over the area within a single photolithographically patterned loop structure, except for the low temperature Rabi (figure 8.7a) and room temperature data (figure 8.9), where it is fixed at the center of the loop. Digital signals to pulse the lasers, and microwaves tones for driving the spin transitions are generated using the Real Digital RFSoC 4x2 running the QICK platform [14] with a custom version of the software and firmware designed for optically-addressable spin qubits. In figure 8.10, the widefield fluorescence image is captured using a Leica DMi8 microscope.

8.10 Data analysis

OADF photon counts (PL) are integrated over the first 300 ns following the rising edge of the 912 nm laser pulse and over multiple experiments. The contrast in figures 8.1e, 8.5, 8.7a, 8.9a, 8.9b, 8.8b, and 8.14 are defined by the following normalization $C = [\mathrm{PL}_{sig.}(\omega) - \mathrm{PL}_{\mathrm{back.}}(\omega)]/\mathrm{PL}_{\mathrm{back.}}(\omega)$, where $\mathrm{PL}_{\mathrm{sig.}}(\omega)$ refers to the PL with microwave output switched on and $\mathrm{PL}_{\mathrm{back.}}(\omega)$ refers to the PL with microwave output switched off. The contrast in figures 8.7b, 8.7c, is defined as $C = \frac{\mathrm{PL}(\theta=-\pi/2)-\mathrm{PL}(\theta=+\pi/2)}{\mathrm{PL}(\theta=-\pi/2)+\mathrm{PL}(\theta=+\pi/2)}$ normalized to the fit maximum, where $\mathrm{PL}(\theta)$ corresponds to the PL signal with the last microwave pulse having rotation angle θ. Finally, the contrast in figure 8.7d is defined as $C = [\mathrm{PL}(\theta = \pi) - \mathrm{PL}(\theta = 0)]/\mathrm{PL}(\theta = 0)$ and in figure 8.9c as $C = [\mathrm{PL}_{\mathrm{sig.}}(\omega_a) - \mathrm{PL}_{\mathrm{sig.}}(\omega_b)]/\mathrm{PL}_{\mathrm{back.}}$, where ω_a and ω_b are fixed frequencies. All stated errors are one standard deviation.

8.11 Sample degradation

The conformational stability of EYFP is interrogated using circular dichroism (CD) spectroscopy. EYFP sample prepared at 100 µM in storage buffer (50 mM, 150 mM NaCl, and 2 mM EDTA; pH = 7.4) is measured hours after purification and another sample of the same concentration is measured after being cooled down to 80 K in our cryostat at 5 mM concentration with 20% DMSO. CD spectra between 180 nm - 260 nm at a scan speed of 100 nm/min, bandwidth of 5 nm are taken using a Jasco J-1500 spectropolarimeter. Figure 8.3a shows the resulting data after averaging over three scans. The spectra exhibit a minimum at 230 nm, indicating that the main secondary structure content of EYFP is a β-sheet configuration. No significant differences are observed between the spectra of the two samples, suggesting that the cooldown and warmup processes used in the experiments did not alter the structure of EYFP.

8.12 Computational methods

The orbital structures in figure 8.1d are the result of TDDFT [63] calculations on the negatively charged model of the EYFP chromophore terminated with methyl groups. The geometry is optimized using the conductor-like polarizable continuum model [64] with a dielectric constant $\epsilon = 4$ to mimic the protein environment. The ground state geometry optimizations for the singlet (S0) and triplet (T1) states are performed using the Gaussian 16 [65] package at B3LYP/def2-TZVP level. The ORCA 5.4.0 package [66] is used for the TDDFT calculations to compute the vertical excitation energies (VEEs). Range-separated hybrid functionals CAM-B3LYP [67] and ωB97X-D3 [68] are used with the B3LYP/def2-TZVP/$\epsilon = 4$ optimized geometries and def2-QZVPP basis sets for the TDDFT calculations. The zero-field splitting calculations for the D and E parameters are performed at the T1 optimized geometry with a series of functionals shown in figure 8.12. The absolute D and

E parameters are calculated using spin-orbit coupling treated at the spin-orbit mean-field (SOMF) theory (as implemented in ORCA 5.4.0 package). The coupled-perturbed method is used for calculating the zero-field splitting tensor with DFT [69].

8.13 TDDFT and ZFS calculations

TDDFT calculations predict the first bright singlet-singlet excitation to occur from the highest occupied molecular orbital (HOMO) to the lowest unoccupied molecular orbital (LUMO), showcasing a $\pi \rightarrow \pi^*$ nature of the transition. This S0→S1 transition corresponds to the experimental absorption at 2.54 eV. Both CAM-B3LYP and ωB97X-D3 predict an energy gap of ∼3.02 eV between the S1 and S0 states. The results overestimate the experimental value, similar to an earlier report for gas phase calculations [70]. The first bright excitation using the triplet optimized geometry occurs for T1→T2, which also corresponds to a $\pi \rightarrow \pi^*$ transition. Although this VEE of ∼1.49 eV also overestimates the experimentally observed triplet-triplet absorption at ∼1.37 eV, it characterizes the T1→T2 transition to involve a singly occupied molecular orbital (SOMO), where the electron is excited from SOMO-2 to SOMO-1.

8.14 Simulation magnetic resonance spectrum

Diagonalizing the Hamiltonian from equation 8.2 provides the $T_z - T_x$, $T_z - T_y$, and $T_y - T_x$ transition frequencies as a function of the magnetic field (B). Importantly, the transition frequencies depend not only on the field strength but also on the molecule's orientation relative to the magnetic field. Assuming that the EYFP molecules are randomly oriented, we sample 10,000 uniformly distributed orientations. To simulate the ODMR spectra in figure 8.5a and 8.5c, we incorporate the single molecule ODMR linewidth (γ). The resonance for a single EYFP molecule is then modeled by a Lorentzian of the form $L(\omega) = \frac{a_{z-y}}{1+(\frac{\omega-\omega_{z-y}}{\gamma})^2} +$

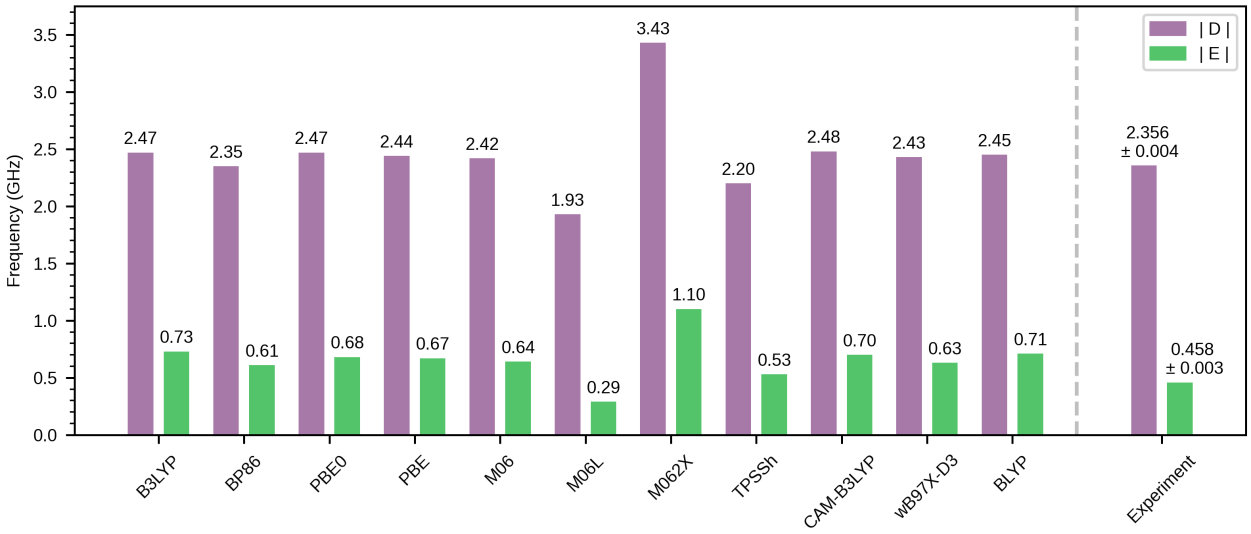


Figure 8.12: The calculated $|D|$ and $|E|$ parameters using TDDFT with B3LYP-optimized geometries and various functionals along with the experimentally measured values.

$\frac{a_{z-x}}{1+(\frac{\omega-\omega_{z-x}}{\gamma})^2}$, where a_{z-x} and a_{z-y} denote the ODMR contrast, and ω_{z-x} and ω_{z-y} the transition frequencies for the $T_z - T_x$ and $T_z - T_y$ transitions, respectively. Note that our model simplifies the fitting by only considering the $T_z - T_x$ and $T_z - T_y$ resonance while omitting the $T_y - T_x$ transition, which has a reduced ODMR contrast and experimental data that overlap with a harmonic of our signal generator. We iteratively optimize the fit parameters D, E, a_{z-x}, a_{z-y}, and γ by minimizing the cost function $C = \sum_i (n(\omega_i) - L(\omega_i))^2$, where $n(\omega_i)$ denotes the experimentally observed ODMR spectra at the following fields: 2.1 mT, 4.5 mT, 6.1 mT, 8.2 mT, and 10 mT (figure 8.5c). We find $D = (2\pi) \times (2.356 \pm 0.004)$ GHz, $E = (2\pi) \times (0.458 \pm 0.003)$ GHz, $a_{z-x} = (0.129 \pm 0.008)$, $a_{z-y} = (0.17 \pm 0.02)$, and $\gamma = (2\pi) \times (33 \pm 4)$ MHz.

8.15 Rabi simulation

We investigate the origin of the Rabi decay shown in figure 8.7a. Interestingly, we observe that the decay time increases with decreasing microwave power (figure 8.8) suggesting that loss in Rabi signal is not caused by dephasing. Instead, we account for inhomogeneous

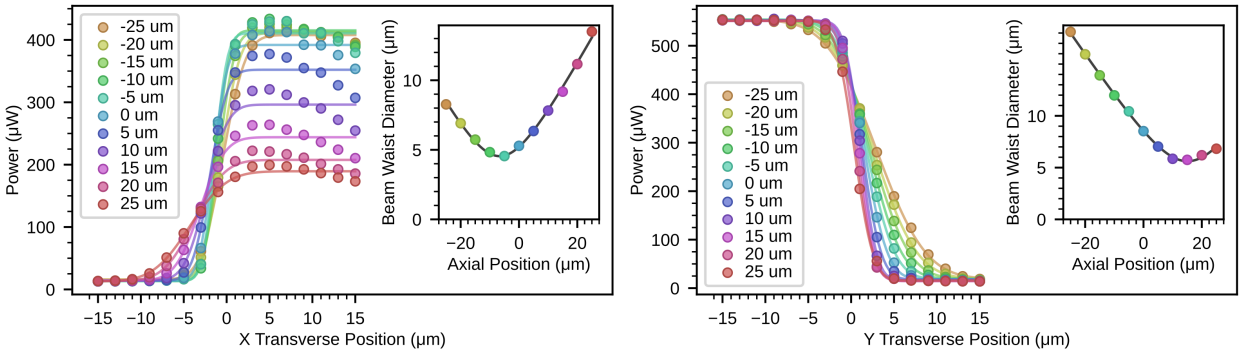


Figure 8.13: In order to characterize the optical beam morphology, the microscope optical assembly is positioned to focus the 488 nm laser spot on a set of optical windows outside the cryostat that mimic the measurement conditions. The power transmitted through a photolithographically-patterned metal edge in the sample plane is measured as a function of transverse displacements in X (left) and Y (right). This measurement is repeated for various axial displacements. The power versus transverse position is fitted to an error function. The beam diameter extracted by the error function fit is then examined as a function of axial displacement (inset). A fit to a hyperbolic profile allows for the extraction of the beam waist and Rayleigh range. The beam appears to display coma or spherical aberration, as well as astigmatism. These aberrations are likely the result of errors in alignment through the cryostat window and sample coverslip.

broadening by sampling over a Gaussian distribution with a $E = (2\pi) \times 33\,\text{MHz}$ standard deviation. In addition, the Rabi frequency depends on the molecule orientation with respect to the microwave drive field. These imperfections result in a fast decay that qualitatively captures our experimental observations (figure 8.8c; a histogram of the Rabi frequencies is shown in the inset). Additionally, the simulation captures the experimental behavior that the decay time increases with decreasing microwave power (figure 8.8d). We note that the inhomogeneous Rabi drive can not be explained by spatial gradients caused by the loop geometry.

8.16 Estimation of number of measured molecules

Knife-edge measurements of the 488 nm laser spot (figure 8.13) estimate a beam waist $\omega_0 = 2.81\,\mu\text{m}$ (the larger between x, y) and Rayleigh range $z_R = 13.19\,\mu\text{m}$. We assume a Gaussian

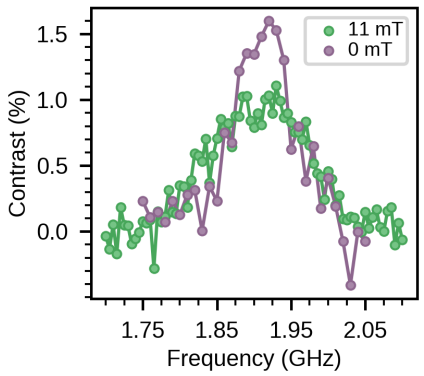


Figure 8.14: ODMR spectra of the T_y-T_z transition at room temperature, exhibiting a broadened linewidth with an applied magnetic field.

beam with intensity $I(r,z) = I_0(\frac{\omega_0}{\omega(z)})^2 \exp\frac{-2r^2}{w(z)^2}$, where $\omega(z) = \omega_0\sqrt{1+(\frac{z}{z_R})^2}$, r is the radial distance, z the distance from focus, and I_0 the maximum intensity. We also assume that the collection and 488 nm excitation beam have the same point-spread function, resulting in a confocal volume $V = \int_{-\infty}^{\infty}\int_0^{2\pi}\int_0^{\infty}\frac{I(r,z)}{I_0}^2 r dr d\phi dz = \frac{z_R(\pi\omega_0)^2}{4}$. Using this volume and a sample concentration of 5 mM, we find that the effective number of molecules in our excitation volume is 773×10^6 molecules. We note that this estimate serves as an upper limit, as we collect into a single-mode fiber, but our imaging system is not diffraction limited due to poor alignment through the cryostat window and sapphire sample coverslip. With diffraction limited imaging, we estimate that we would measure about 810× fewer molecules with approximately the same brightness, providing about 28× better sensitivity than we estimate in this work.

8.17 Sensitivity estimation

The minimum signal that can be detected when integrating for a duration, T, is given by $\frac{S_T}{\sigma_T} = 1$, where S_T denotes the signal and σ_T the standard deviation of S_T. In the following, the system's response is linear with respect to a small field (δB) such that $\frac{dS_T/dB \times \delta B}{\sigma_T} = 1$. Therefore, the minimum field that can be detected is

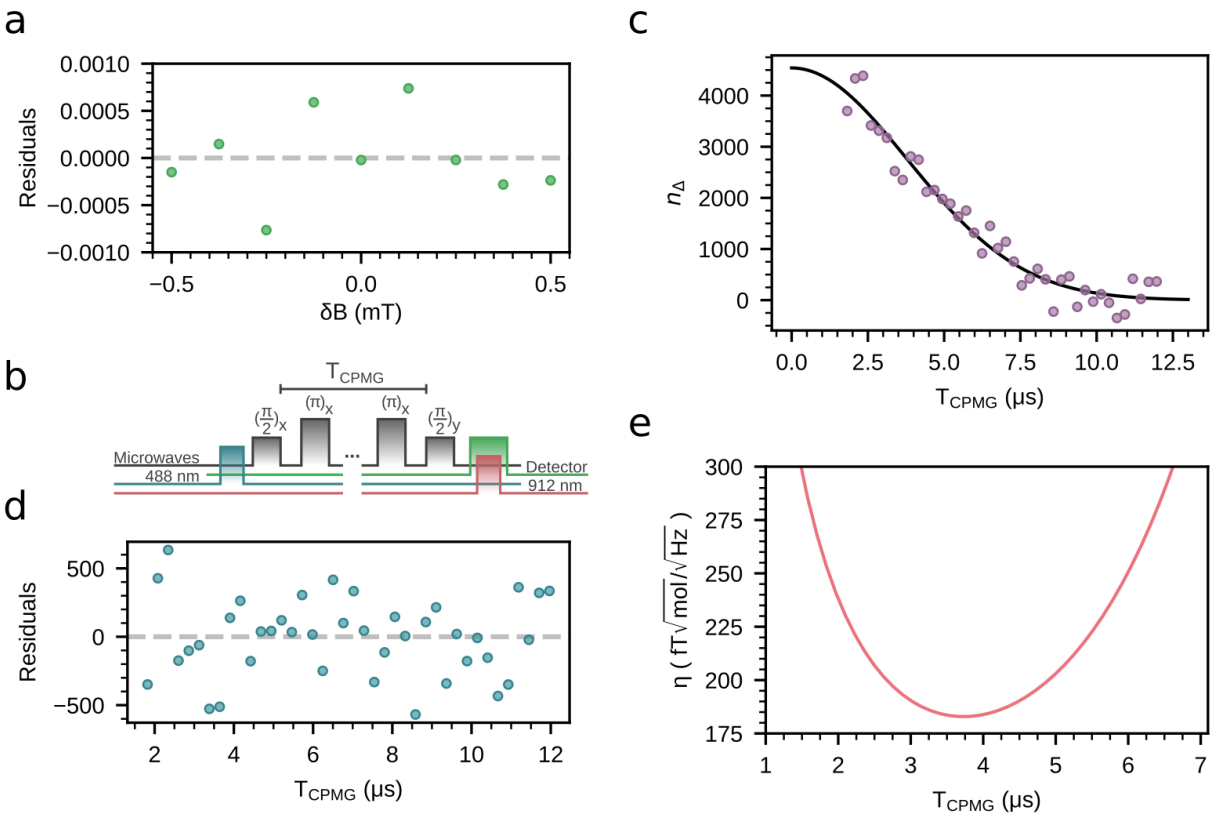


Figure 8.15: **(a)** Residuals from figure 8.9c used to estimate the DC sensitivity at room temperature. **(b)** CPMG sequence used for AC magnetic field sensing. **(c)** $n_{\delta,250k}$ and its fit (black). **(d)** The residuals estimated from $n_{\delta,250k}$ and its fit. **(e)** The estimated η. Panel (c) is measured at 80 K.

$$\delta B_{min}(T) = \frac{\sigma_T}{dS_T/dB}$$

(eq.-3),

where $\frac{dS_T}{dB}$ is maximized. Assuming the measurement is shot-noise limited, the sensitivity is $\eta = \delta B_{\min}\sqrt{T}$ [62].

8.17.1 DC sensitivity (293 K)

To quantify the DC field sensitivity, we measure the difference of the photoluminescence (PL) at $\omega_a = (2\pi) \times 3.54\,\text{GHz}$ and $\omega_b = (2\pi) \times 3.43\,\text{GHz}$, and normalize the signal to the

photoluminescence in the absence of microwaves ($\mathrm{PL_{back.}}$). The resulting signal is then given by $C_T = [\mathrm{PL_{sig.}}(\omega_a) - \mathrm{PL_{sig.}}(\omega_b)]/\mathrm{PL_{back.}}$. The fit has a slope of $dS_T/dB_0 = 5.0\,\mathrm{T}^{-1}$ and the residuals (figure 8.15a) have a standard deviation $\sigma_T = 4.6\times10^{-3}$ yielding a sensitivity of $\eta = 2.7\,\mathrm{mTHz}^{-1/2}$. Assuming an excitation volume of $100\,\mu\mathrm{m}^3$ and an EYFP concentration of 5 mM, which translates into 773×10^6 molecules, we find a room-temperature DC magnetic field sensitivity of $98\,\mathrm{pTmol}^{1/2}\mathrm{Hz}^{-1/2}$.

8.17.2 AC sensitivity (80 K)

AC sensing of small fields can be done using the CPMG sequence shown in figure 8.15b. The signal of a single CPMG sequence is then given by $S_\pm = \frac{n_\Delta}{2}(1 \pm \sin(\phi)) + \frac{n_\Sigma}{2}$, where n_Δ denotes the difference in photon counts between the T_z and T_x state, n_Σ their average, and the sign denotes the phase of the last $\pi/2$-pulse. Assuming a sinusoidal magnetic field with amplitude δB_{AC}, frequency $T_{\mathrm{CPMG}}/(2N)$ and in phase with the CPMG sequence, we can write the accumulated phase as $\phi = \gamma\delta B_{\mathrm{AC}} T_{\mathrm{CPMG}} W$, with $W = 2/\pi$. The detected signal is then given by $S = S_+ - S_- = n_\Delta \sin(2\gamma\delta B_{\mathrm{AC}} T_{\mathrm{CPMG}}/\pi)$ and the sensitivity by $\eta = \frac{\pi}{2(n_\Delta/\sigma_n)\gamma_{\mathrm{eff}} T_{\mathrm{CPMG}}}\sqrt{2(T_{\mathrm{CPMG}} + T_0)}$, where σ_n denotes the standard deviation of n_Δ and T_0 the experimental overhead time. The factor $\sqrt{2}$ originates from measuring n_Δ with two CPMG sequences. To experimentally estimate the AC sensitivity of EYFP, we integrated the signal over 250,000 experiments. We fit the difference in photon counts $n_{\Delta,250k} = 4541 \times \exp(-(T_{\mathrm{CPMG}}/5.35\,\mu\mathrm{s}^2)$ as a function of T_{CPMG} (figure 8.15c) and $\sigma_{n,250k} = 288$ from the corresponding residual (figure 8.15d). We can now estimate for a single experiment that $n_\Delta = \frac{n_{\Delta,250k}}{250{,}000}$ and $\sigma_n = \frac{\sigma_{n,250k}}{\sqrt{250{,}000}}$. Under these conditions, we find $T_{\mathrm{CPMG}} = 3.68\,\mu\mathrm{s}$ to be the optimal sensing duration (figure 8.15e). Assuming an effective gyromagnetic ratio of $\gamma_{\mathrm{eff}} = (2\pi) \times 7.63\,\mathrm{GHz\,T}^{-1}$ (i.e., operating at $B = 4.65\,\mathrm{mT}$) and using $T_0 = 60\,\mu\mathrm{s}$, this results in a field sensitivity of $\eta = 5.11\,\mu\mathrm{THz}^{-1/2}$. Given that we measured approximately 773×10^6 molecules, this translates into a sensitivity of $183\,\mathrm{fTmol}^{1/2}\mathrm{Hz}^{-1/2}$.

8.18 Limit of detection: NMR sensing

In this section we consider a thought experiment where we calculate the proton sensitivity of an ensemble of N fusion proteins each consisting of a EYFP protein conjugated to a target protein that contains a single ^{1}H nuclear spin. This ^{1}H nuclear spin is 5 nm separated from the qubit and produces a local magnetic field of $\delta B = 20\,\mathrm{nT}$ at the location of the chromophore. The field strength δB is dominated by the target ^{1}H spin in the fusion protein, and other ^{1}H spins are significantly further away and do not contribute to the signal. Starting from the AC sensitivity calculation $\eta = \frac{\pi}{2(n_\Delta/\sigma_n)\gamma_{\mathrm{eff}}T_{\mathrm{CPMG}}}\sqrt{2(T_{\mathrm{CPMG}}+T_0)}$, we derive the limit of detection for NMR spectroscopy. However, in NMR only a small fraction of nuclear spins are polarized. Using the nuclear spin polarization, p, the overall signal is reduced to $S = pn_\Delta \sin(2\gamma\delta B_{\mathrm{AC}}T_{\mathrm{CPMG}}/\pi)$, resulting in a sensitivity of $\eta = \frac{\pi}{2(pn_\Delta/\sigma_n)\gamma_{\mathrm{eff}}T_{\mathrm{CPMG}}}\sqrt{2(T_{\mathrm{CPMG}}+T_0)} = \frac{1}{p}\eta$. This results in a polarization-adjusted sensitivity of $\eta_p = \frac{1}{p}183\,\mathrm{fTmol}^{1/2}\mathrm{Hz}^{-1/2}$ (see main text), allowing us to detect a magnetic field of $\frac{1}{\sqrt{NT}}\eta_p$. Solving for N we find a limit of detection of $N = \frac{1}{T}(\eta_p\frac{1}{\delta B})^2 = \frac{1}{T}\frac{80}{p}\mathrm{pM\,Hz}$.

CHAPTER 9

METASTABLE TRIPLET DYNAMICS

The key to creating a good spin sensor in a molecule with a metastable triplet is the control of the triplet state population. In order to do that effectively, we should develop a quantitative understanding of the molecule's behavior. We can model the interaction of laser pulses with the molecule using rate equations.

9.1 Initialization

Let's consider the initialization process that populates the metastable triplet state.

9.1.1 3-level model

Figure 9.1 shows a 3-level system that represents a metastable triplet molecule. We apply a laser that excites the S_0 state with a rate a. Decay from S_1 to S_0 occurs at a rate b. Intersystem crossing (c) and reverse intersystem crossing (f) populate and depopulate the triplet state, respectively.

We can model this system using the rate equation

$$\frac{d}{dt}\begin{bmatrix} S_0 \\ S_1 \\ T_1 \end{bmatrix} = \begin{bmatrix} -a & b & f \\ a & -(b+c) & 0 \\ 0 & c & -f \end{bmatrix} \begin{bmatrix} S_0 \\ S_1 \\ T_1 \end{bmatrix}, \tag{9.1}$$

where S_0, S_1, and T_1 represent the population fractions in those states. If we let $S_0 + S_1 + T_1 = 1$, we can find the steady-state condition of the system by setting $\frac{d}{dt}S_0 = 0$, $\frac{d}{dt}S_1 = 0$, $\frac{d}{dt}T_1 = 0$:

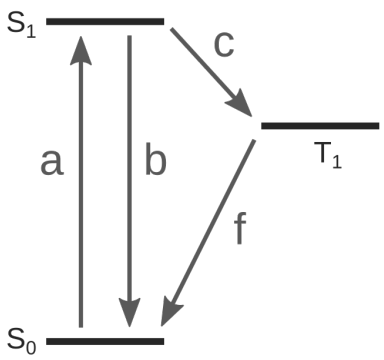


Figure 9.1: Simple model representing a molecule with a metastable triplet state.

$$\begin{bmatrix} -a & b & f \\ a & -(b+c) & 0 \\ 0 & c & -f \\ 1 & 1 & 1 \end{bmatrix} \begin{bmatrix} S_0 \\ S_1 \\ T_1 \end{bmatrix} = \begin{bmatrix} 0 \\ 0 \\ 0 \\ 1 \end{bmatrix}, \tag{9.2}$$

and solving algebraically

$$\begin{bmatrix} S_0 \\ S_1 \\ T_1 \end{bmatrix} = \begin{bmatrix} \frac{f(b+c)}{f(a+b+c)+ac} \\ \frac{af}{f(a+b+c)+ac} \\ \frac{ac}{f(a+b+c)+ac} \end{bmatrix}. \tag{9.3}$$

The triplet yield, ϕ_T, is defined as $\phi_T = \frac{c}{c+b}$. For EYFP, $\phi_T \approx 0.003$ [12] and, therefore, $b >> c$. If we further assume the laser excitation rate, a, is much larger than b, we find that

$$\begin{bmatrix} S_0 \\ S_1 \\ T_1 \end{bmatrix} = \begin{bmatrix} \frac{f(b+c)}{f(a+b+c)+ac} \\ \frac{af}{f(a+b+c)+ac} \\ \frac{ac}{f(a+b+c)+ac} \end{bmatrix} \approx \begin{bmatrix} \frac{f}{f+c}\frac{b}{a} \\ \frac{af}{af+ac} \\ \frac{ac}{af+ac} \end{bmatrix} \approx \begin{bmatrix} 0 \\ \frac{f}{f+c} \\ \frac{c}{f+c} \end{bmatrix}. \tag{9.4}$$

This makes some intuitive sense: the steady-state population in T_1 is the fractional strength of the ISC, which populates the triplet, relative to the RISC, which depopulates

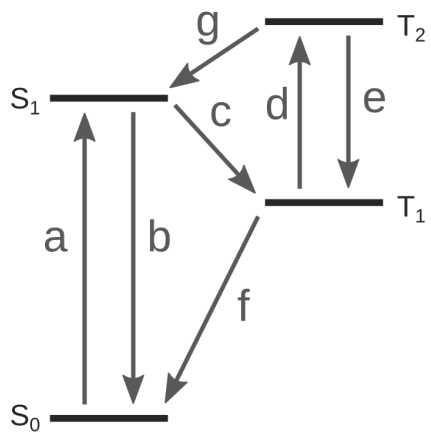


Figure 9.2: Model representing a molecule with a metastable triplet state.

the triplet. Notice that if b is significant compared to a, the triplet population will only get smaller. Therefore, in order to maximize the triplet population, we want to be in a "saturating" condition, where $a >> b, c$.

For EGFP, $f = 1/3\,\text{ms}$ and $b = 1/3\,\text{ns}$ [2]. We can solve $\phi_T = \frac{c}{c+b}$ for $c = b\frac{\phi_T}{1-\phi_T} \approx 1/1\,\mu\text{s}$. This would imply that the triplet population is nearly 1 under saturating conditions. In practice, this is not the case. We can see why if we consider a more sophisticated model.

9.1.2 4-level model

Let's now consider the impact of additional higher-lying triplet states on the initialization process. In practice, there could be any number of these triplets, but, for simplicity, let's treat these additional states as a single state, T_2, as shown in figure 9.2. We now have an additional laser pumping rate, d, which represents the pumping of the triplet-triplet transition by the same laser that pumps the singlet transition. Furthermore, we have a relaxation rate, e, associated with the T_2 state, and g, the reverse intersystem-crossing rate from the T_2 state. We can write out the steady state condition as

$$\frac{d}{dt}\begin{bmatrix} S_0 \\ S_1 \\ T_1 \\ T_2 \end{bmatrix} = \begin{bmatrix} -a & b & f & 0 \\ a & -(b+c) & 0 & g \\ 0 & c & -(d+f) & e \\ 0 & 0 & d & -(e+g) \\ 1 & 1 & 1 & 1 \end{bmatrix} \begin{bmatrix} S_0 \\ S_1 \\ T_1 \\ T_2 \end{bmatrix} = \begin{bmatrix} 0 \\ 0 \\ 0 \\ 0 \\ 1 \end{bmatrix}. \tag{9.5}$$

Solving, we find that $T_2 = \frac{d}{e+g}T_1$ and

$$T_1 = \frac{ac(e+g)}{(ac + f(a+b))(e+g) + dg(a+b) + acd}. \tag{9.6}$$

Let's assume that $a >> b$ and $c >> f$ so that

$$T_1 = \frac{c(e+g)}{c(e+g) + d(c+g)}. \tag{9.7}$$

In the case that the singlet yield, $\frac{g}{e+g}$, is low, almost all of the T_2 population will decay back down to the T_1 state after the laser has switched off. Therefore, we can use the combined triplet population, $T_1 + T_2$ as a proxy for the population in the T_1 state after the initialization laser pulse. Therefore, the triplet population

$$T_1 + T_2 = \frac{c(d+e+g)}{c(d+e+g) + dg}. \tag{9.8}$$

If we make a similar assumption to the 3-level system model such that $d >> e >> g$, we are left with a similar result

$$T_1 + T_2 = \frac{c}{c+g}. \tag{9.9}$$

Again, we see that the triplet population is simply the fractional strength of the ISC rate versus the RISC rate. However, g is likely larger than c, which suggests that the triplet population may be much less than 1. We can also see from equation 9.8 that if we can make

$d = 0$, then $T_1 + T_2 = 1$. This suggests that the key to achieving a high triplet population is to minimize the rate d, which is the parasitic pumping of the triplet transitions by the initialization laser.

REFERENCES

1. AAT Bioquest, I. *Spectrum [EYFP]* https://www.aatbio.com/fluorescence-excitation-emission-spectrum-graph-viewer/eyfp. Accessed: 2025-04-21. 2025.

2. Byrdin, M., Duan, C., Bourgeois, D. & Brettel, K. A Long-Lived Triplet State Is the Entrance Gateway to Oxidative Photochemistry in Green Fluorescent Proteins. *Journal of the American Chemical Society* **140,** 2897–2905. doi:10.1021/jacs.7b12755 (Feb. 28, 2018).

3. Wachter, R. M., Elsliger, M. A., Kallio, K., Hanson, G. T. & Remington, S. J. Structural basis of spectral shifts in the yellow-emission variants of green fluorescent protein. *Structure (London, England: 1993)* **6,** 1267–1277. doi:10.1016/s0969-2126(98)00127-0 (Oct. 15, 1998).

4. Reid, B. G. & Flynn, G. C. Chromophore Formation in Green Fluorescent Protein. *Biochemistry* **36,** 6786–6791. doi:10.1021/bi970281w (June 1, 1997).

5. Creemers, T. M. H., Lock, A. J., Subramaniam, V., Jovin, T. M. & Völker, S. Photophysics and optical switching in green fluorescent protein mutants. *Proceedings of the National Academy of Sciences* **97.** Publisher: Proceedings of the National Academy of Sciences, 2974–2978. doi:10.1073/pnas.97.7.2974 (Mar. 28, 2000).

6. Chattoraj, M., King, B. A., Bublitz, G. U. & Boxer, S. G. Ultra-fast excited state dynamics in green fluorescent protein: multiple states and proton transfer. *Proceedings of the National Academy of Sciences* **93,** 8362–8367. doi:10.1073/pnas.93.16.8362 (Aug. 6, 1996).

7. Rodriguez, E. A. *et al.* The Growing and Glowing Toolbox of Fluorescent and Photoactive Proteins. *Trends in Biochemical Sciences* **42,** 111–129. doi:10.1016/j.tibs.2016.09.010 (Feb. 2017).

8. Cormack, B. P., Valdivia, R. H. & Falkow, S. FACS-optimized mutants of the green fluorescent protein (GFP). *Gene* **173,** 33–38. doi:10.1016/0378-1119(95)00685-0 (1996).

9. Matz, M. V. *et al.* Fluorescent proteins from nonbioluminescent Anthozoa species. *Nature Biotechnology* **17,** 969–973. doi:10.1038/13657 (Oct. 1, 1999).

10. Miesenböck, G., De Angelis, D. A. & Rothman, J. E. Visualizing secretion and synaptic transmission with pH-sensitive green fluorescent proteins. *Nature* **394,** 192–195. doi:10.1038/28190 (July 1998).

11. Akerboom, J. *et al.* Genetically encoded calcium indicators for multi-color neural activity imaging and combination with optogenetics. *Frontiers in Molecular Neuroscience* **6.** doi:10.3389/fnmol.2013.00002 (2013).

12. Peng, B. *et al.* Optically Modulated and Optically Activated Delayed Fluorescent Proteins through Dark State Engineering. *The Journal of Physical Chemistry B* **125,** 5200–5209. doi:10.1021/acs.jpcb.1c00649 (May 27, 2021).

13. Stefanazzi, L. *et al.* The QICK (Quantum Instrumentation Control Kit): Readout and control for qubits and detectors. *Review of Scientific Instruments* **93,** 044709. doi:10.1063/5.0076249 (Apr. 2022).

14. Ding, C. *et al.* Experimental advances with the QICK (Quantum Instrumentation Control Kit) for superconducting quantum hardware. *Physical Review Research* **6,** 013305. doi:10.1103/PhysRevResearch.6.013305 (Mar. 20, 2024).

15. Feder, J. S. *et al.* A fluorescent-protein spin qubit. *arXiv preprint,* quant–ph 2411.16835. doi:10.48550/arXiv.2411.16835 (2024).

16. Casola, F., Van Der Sar, T. & Yacoby, A. Probing condensed matter physics with magnetometry based on nitrogen-vacancy centres in diamond. *Nature Reviews Materials* **3,** 17088. doi:10.1038/natrevmats.2017.88 (Jan. 4, 2018).

17. Awschalom, D. D., Hanson, R., Wrachtrup, J. & Zhou, B. B. Quantum technologies with optically interfaced solid-state spins. *Nature Photonics* **12,** 516–527. doi:10.1038/s41566-018-0232-2 (Sept. 2018).

18. Schirhagl, R., Chang, K., Loretz, M. & Degen, C. L. Nitrogen-vacancy centers in diamond: nanoscale sensors for physics and biology. *Annual Review of Physical Chemistry* **65,** 83–105. doi:10.1146/annurev-physchem-040513-103659 (Apr. 2014).

19. Aslam, N. *et al.* Quantum sensors for biomedical applications. *Nature Reviews Physics* **5,** 157–169. doi:10.1038/s42254-023-00558-3 (Feb. 3, 2023).

20. Du, J., Shi, F., Kong, X., Jelezko, F. & Wrachtrup, J. Single-molecule scale magnetic resonance spectroscopy using quantum diamond sensors. *Reviews of Modern Physics* **96,** 025001. doi:10.1103/RevModPhys.96.025001 (May 8, 2024).

21. Griffin, B. A., Adams, S. R. & Tsien, R. Y. Specific Covalent Labeling of Recombinant Protein Molecules Inside Live Cells. *Science* **281,** 269–272. doi:10.1126/science.281.5374.269 (July 10, 1998).

22. Tsien, R. Y. & Miyawaki, A. Seeing the machinery of live cells. *Science* **280,** 1954–1955. doi:10.1126/science.280.5371.1954 (June 19, 1998).

23. Miyawaki, A. Proteins on the move: insights gained from fluorescent protein technologies. *Nature Reviews Molecular Cell Biology* **12,** 656–668. doi:10.1038/nrm3199 (Oct. 2011).

24. Balasubramanian, G. *et al.* Nanoscale imaging magnetometry with diamond spins under ambient conditions. *Nature* **455,** 648–651. doi:10.1038/nature07278 (Oct. 2008).

25. Degen, C. L. Scanning magnetic field microscope with a diamond single-spin sensor. *Applied Physics Letters* **92,** 243111. doi:10.1063/1.2943282 (June 16, 2008).

26. Maze, J. R. *et al.* Nanoscale magnetic sensing with an individual electronic spin in diamond. *Nature* **455,** 644–647. doi:10.1038/nature07279 (Oct. 2008).

27. Dolde, F. *et al.* Electric-field sensing using single diamond spins. *Nature Physics* **7,** 459–463. doi:10.1038/nphys1969 (June 2011).

28. Toyli, D. M., De Las Casas, C. F., Christle, D. J., Dobrovitski, V. V. & Awschalom, D. D. Fluorescence thermometry enhanced by the quantum coherence of single spins in diamond. *Proceedings of the National Academy of Sciences* **110,** 8417–8421. doi:10.1073/pnas.1306825110 (May 21, 2013).

29. Kucsko, G. *et al.* Nanometre-scale thermometry in a living cell. *Nature* **500,** 54–58. doi:10.1038/nature12373 (Aug. 2013).

30. Neumann, P. *et al.* High-Precision Nanoscale Temperature Sensing Using Single Defects in Diamond. *Nano Letters* **13,** 2738–2742. doi:10.1021/nl401216y (June 12, 2013).

31. Bhattacharyya, P. *et al.* Imaging the Meissner effect in hydride superconductors using quantum sensors. *Nature* **627,** 73–79. doi:10.1038/s41586-024-07026-7 (Mar. 7, 2024).

32. Fu, R. R. *et al.* Solar nebula magnetic fields recorded in the Semarkona meteorite. *Science* **346,** 1089–1092. doi:10.1126/science.1258022 (Nov. 28, 2014).

33. Tetienne, J.-P. *et al.* Nanoscale imaging and control of domain-wall hopping with a nitrogen-vacancy center microscope. *Science* **344,** 1366–1369. doi:10.1126/science.1250113 (June 20, 2014).

34. Andersen, T. I. *et al.* Electron-phonon instability in graphene revealed by global and local noise probes. *Science* **364,** 154–157. doi:10.1126/science.aaw2104 (Apr. 12, 2019).

35. Cai, E. *et al.* Stable Small Quantum Dots for Synaptic Receptor Tracking on Live Neurons. *Angewandte Chemie International Edition* **53,** 12484–12488. doi:10.1002/anie.201405735 (Nov. 10, 2014).

36. Knowles, H. S., Kara, D. M. & Atatüre, M. Observing bulk diamond spin coherence in high-purity nanodiamonds. *Nature Materials* **13,** 21–25. doi:10.1038/nmat3805 (Jan. 2014).

37. Andrich, P. *et al.* Engineered Micro- and Nanoscale Diamonds as Mobile Probes for High-Resolution Sensing in Fluid. *Nano Letters* **14,** 4959–4964. doi:10.1021/nl501208s (Sept. 10, 2014).

38. Wrachtrup, J., von Borczyskowski, C., Bernard, J., Orrit, M. & Brown, R. Optical detection of magnetic resonance in a single molecule. *Nature* **363,** 244–245. doi:10.1038/363244a0 (May 1993).

39. Köhler, J. *et al.* Magnetic resonance of a single molecular spin. *Nature* **363,** 242–244. doi:10.1038/363242a0 (May 1993).

40. Mena, A. *et al.* Room-Temperature Optically Detected Coherent Control of Molecular Spins. *Physical Review Letters* **133,** 120801. doi:10.1103/PhysRevLett.133.120801 (Sept. 16, 2024).

41. Singh, H. *et al. Room-temperature quantum sensing with photoexcited triplet electrons in organic crystals* Dec. 23, 2024. doi:10.48550/arXiv.2402.13898.

42. Bayliss, S. L. *et al.* Optically addressable molecular spins for quantum information processing. *Science* **370,** 1309–1312. doi:10.1126/science.abb9352 (Dec. 11, 2020).

43. Shin, A. J. *et al.* Toward liquid cell quantum sensing: Ytterbium complexes with ultranarrow absorption. *Science* **385,** 651–656. doi:10.1126/science.adf7577 (Oct. 8, 2024).

44. Serrano, D. *et al.* Ultra-narrow optical linewidths in rare-earth molecular crystals. *Nature* **603,** 241–246. doi:10.1038/s41586-021-04316-2 (Mar. 10, 2022).

45. Gorgon, S. *et al.* Reversible spin-optical interface in luminescent organic radicals. *Nature* **620,** 538–544. doi:10.1038/s41586-023-06222-1 (Aug. 17, 2023).

46. Kopp, S. M. *et al.* Luminescent Organic Triplet Diradicals as Optically Addressable Molecular Qubits. *Journal of the American Chemical Society* **146,** 27935–27945. doi:10.1021/jacs.4c11116 (Oct. 9, 2024).

47. Rane, L. *et al.* Light-Induced Forward and Reverse Intersystem Crossing in Green Fluorescent Proteins at Cryogenic Temperatures. *The Journal of Physical Chemistry B* **127,** 5046–5054. doi:10.1021/acs.jpcb.3c02971 (June 8, 2023).

48. Ringemann, C. *et al.* Enhancing Fluorescence Brightness: Effect of Reverse Intersystem Crossing Studied by Fluorescence Fluctuation Spectroscopy. *ChemPhysChem* **9,** 612–624. doi:10.1002/cphc.200700596 (Mar. 14, 2008).

49. Schweiger, A. & Jeschke, G. *Principles of Pulse Electron Paramagnetic Resonance* doi:10.1093/oso/9780198506348.001.0001 (Oxford University Press, 2001).

50. Bayliss, S. L. *et al.* Enhancing Spin Coherence in Optically Addressable Molecular Qubits through Host-Matrix Control. *Physical Review X* **12,** 031028. doi:10.1103/PhysRevX.12.031028 (Aug. 18, 2022).

51. Ramsey, N. F. A Molecular Beam Resonance Method with Separated Oscillating Fields. *Physical Review* **78,** 695–699. doi:10.1103/PhysRev.78.695 (June 15, 1950).

52. Meiboom, S. & Gill, D. Modified Spin-Echo Method for Measuring Nuclear Relaxation Times. *Review of Scientific Instruments* **29,** 688–691. doi:10.1063/1.1716296 (Aug. 1, 1958).

53. Medford, J. *et al.* Scaling of Dynamical Decoupling for Spin Qubits. *Physical Review Letters* **108,** 086802. doi:10.1103/PhysRevLett.108.086802 (Feb. 23, 2012).

54. Boyd, M. M. *et al.* Sr 87 Lattice Clock with Inaccuracy below 10 - 15. *Physical Review Letters* **98,** 083002. doi:10.1103/PhysRevLett.98.083002 (Feb. 21, 2007).

55. Bajar, B., Wang, E., Zhang, S., Lin, M. & Chu, J. A Guide to Fluorescent Protein FRET Pairs. *Sensors* **16,** 1488. doi:10.3390/s16091488 (Sept. 14, 2016).

56. Bucher, D. B., Glenn, D. R., Park, H., Lukin, M. D. & Walsworth, R. L. Hyperpolarization-Enhanced NMR Spectroscopy with Femtomole Sensitivity Using Quantum Defects in Diamond. *Physical Review X* **10,** 021053. doi:10.1103/PhysRevX.10.021053 (June 9, 2020).

57. Ward, R. *et al.* EPR distance measurements in deuterated proteins. *Journal of Magnetic Resonance* **207,** 164–167. doi:10.1016/j.jmr.2010.08.002 (Nov. 2010).

58. El Mkami, H., Ward, R., Bowman, A., Owen-Hughes, T. & Norman, D. G. The spatial effect of protein deuteration on nitroxide spin-label relaxation: Implications for EPR distance measurement. *Journal of Magnetic Resonance* **248,** 36–41. doi:10.1016/j.jmr.2014.09.010 (Nov. 2014).

59. Byrdin, M. & Byrdina, S. *Impact of Triplet State Population on GFP-type Fluorescence and Photobleaching* Feb. 22, 2024. doi:10.1101/2024.02.19.580967.

60. Ha, T. & Tinnefeld, P. Photophysics of Fluorescent Probes for Single-Molecule Biophysics and Super-Resolution Imaging. *Annual Review of Physical Chemistry* **63,** 595–617. doi:10.1146/annurev-physchem-032210-103340 (May 2012).

61. Rothemund, P. W. K. Folding DNA to create nanoscale shapes and patterns. *Nature* **440,** 297–302. doi:10.1038/nature04586 (Mar. 16, 2006).

62. Schiemann, O. *et al.* A PELDOR-Based Nanometer Distance Ruler for Oligonucleotides. *Journal of the American Chemical Society* **126,** 5722–5729. doi:10.1021/ja0393877 (May 1, 2004).

63. Gross, E. K. U. & Kohn, W. in *Advances in Quantum Chemistry* (ed Löwdin, P.-O.) 255–291 (Academic Press, Jan. 1, 1990). doi:10.1016/S0065-3276(08)60600-0.

64. Cossi, M., Rega, N., Scalmani, G. & Barone, V. Energies, structures, and electronic properties of molecules in solution with the C-PCM solvation model. *Journal of Compu-*

tational Chemistry **24.** _eprint: https://onlinelibrary.wiley.com/doi/pdf/10.1002/jcc.10189, 669–681. doi:10.1002/jcc.10189 (2003).

65. Frisch, M. J. *et al. Gaussian˜16 Revision C.01* Gaussian Inc. Wallingford CT. 2016.

66. Neese, F. The ORCA program system. *WIREs Computational Molecular Science* **2.** _eprint: https://onlinelibrary.wiley.com/doi/pdf/10.1002/wcms.81, 73–78. doi:10.1002/wcms.81 (2012).

67. Yanai, T., Tew, D. P. & Handy, N. C. A new hybrid exchange–correlation functional using the Coulomb-attenuating method (CAM-B3LYP). *Chemical Physics Letters* **393,** 51–57. doi:10.1016/j.cplett.2004.06.011 (July 21, 2004).

68. Lin, Y.-S., Li, G.-D., Mao, S.-P. & Chai, J.-D. Long-Range Corrected Hybrid Density Functionals with Improved Dispersion Corrections. *Journal of Chemical Theory and Computation* **9.** Publisher: American Chemical Society, 263–272. doi:10.1021/ct300715s (Jan. 8, 2013).

69. Neese, F. Calculation of the zero-field splitting tensor on the basis of hybrid density functional and Hartree-Fock theory. *The Journal of Chemical Physics* **127,** 164112. doi:10.1063/1.2772857 (Oct. 30, 2007).

70. Filippi, C., Zaccheddu, M. & Buda, F. Absorption Spectrum of the Green Fluorescent Protein Chromophore: A Difficult Case for ab Initio Methods? *Journal of Chemical Theory and Computation* **5.** Publisher: American Chemical Society, 2074–2087. doi:10.1021/ct900227j (Aug. 11, 2009).